INTERNATIONAL JOURNAL OF CLIMATOLOGY
Int. J. Climatol. **37**: 3175–3196 (2017)
Published online 4 November 2016 in Wiley Online Library
(wileyonlinelibrary.com) DOI: 10.1002/joc.4922

RMetS
Royal Meteorological Society

The Andes Cordillera. Part IV: spatio-temporal freshwater run-off distribution to adjacent seas (1979–2014)

Sebastian H. Mernild,[a,b]* Glen E. Liston,[c] Christopher Hiemstra,[d] Andrew P. Beckerman,[e] Jacob C. Yde[b] and James McPhee[f]

[a] *Antarctic and Sub-Antarctic Program, Universidad de Magallanes, Punta Arenas, Chile*
[b] *Faculty of Engineering and Science, Sogn og Fjordane University College, Sogndal, Norway*
[c] *Cooperative Institute for Research in the Atmosphere, Colorado State University, Fort Collins, CO, USA*
[d] *U.S. Army Cold Regions Research and Engineering Laboratory, Ft. Wainwright, AK, USA*
[e] *Department of Animal and Plant Sciences, University of Sheffield, UK*
[f] *Department of Civil Engineering and Advanced Mining Technology Center, Facultad de Ciencias Fisicas y Matemáticas, Universidad de Chile, Santiago, Chile*

ABSTRACT: The spatio-temporal freshwater river run-off pattern from individual basins, including their run-off magnitude and change (1979/1980–2013/2014), was simulated for the Andes Cordillera west of the Continental Divide in an effort to understand run-off variations and freshwater fluxes to adjacent fjords, Pacific Ocean, and Drake Passage. The modelling tool SnowModel/HydroFlow was applied to simulate river run-off at 3-h intervals to resolve the diurnal cycle and at 4-km horizontal grid increments using atmospheric forcing from NASA Modern-Era Retrospective Analysis for Research and Applications (MERRA) data sets. Simulated river run-off hydrographs were verified against independent observed hydrographs. For the domain, 86% of the simulated run-off originated from rain, 12% from snowmelt, and 2% from ice melt, whereas for Chile, the water-source distribution was 69, 24, and 7%, respectively. Along the Andes Cordillera, the 35-year mean basin outlet-specific run-off ($L\,s^{-1}\,km^{-2}$) showed a characteristic regional hourglass shape pattern with highest run-off in both Colombia and Ecuador and in Patagonia, and lowest run-off in the Atacama Desert area. An Empirical Orthogonal Function analysis identified correlations between the spatio-temporal pattern of run-off and flux to the El Niño Southern Oscillation Index and to the Pacific Decadal Oscillation.

KEY WORDS Andes Cordillera; freshwater run-off; HydroFlow; modelling; NASA MERRA; river; South America

Received 9 May 2016; Revised 26 September 2016; Accepted 27 September 2016

1. Introduction

River run-off integrates a response of the watershed to precipitation, snow and glacier presence, groundwater flow, and other hydrometeorological processes (e.g. Liston and Mernild, 2012; Bliss *et al.*, 2014). Snow, glaciers, and underground reservoirs store and release melt water on a range of timescales that control downstream river run-off regimes (Jansson *et al.*, 2003; Hock *et al.*, 2005; Bliss *et al.*, 2014). In most cases, the largest meltwater contribution occurs during annual springtime snowmelt. On a longer timescale of years, glaciers represent a longer-term storage influenced by warmer periods when mass balances are negative, or cooler periods when they are positive. Given shifts in snow and rain contributions as well as glacial mass balances (Vaughan *et al.*, 2013), accurate estimates of snow and glacial melt inputs to the hydrological budget are needed.

For South America, modelling tools offer potential to enhance the limited streamflow observational record at high elevation Andean river basins. For 50 river basins in Colombia, Poveda *et al.* (2001) emphasized that the effects of coarse-scale natural atmospheric variability above the Pacific Ocean – the multivariate El Niño Southern Oscillation (ENSO) (Wolter and Timlin, 2011) – are stronger for river run-off than for precipitation, owing to concomitant effects of soil moisture content and evapotranspiration. However, between latitudes 30° and 35°S, El Niño events have a strong tendency to be positively linked to annual precipitation, and negatively linked during La Niña events (Rutllant and Fuenzalida, 1991; Escobar *et al.*, 1995; Montecinos and Aceituno, 2002; Garreaud, 2009; Wolter and Timlin, 2011).

Fleischbein *et al.* (2006) estimated the water budget for three river basins in Ecuador (4°S) (1998–2002) based on observations and modelled surface flow, and showed that ~40% of the run-off came from rainfall. Crespo *et al.* (2011) analysed the rainfall-run-off relation of 13 intensively monitored micro-basins in the Andes of southern Ecuador (4°S), and showed that the annual amount of run-off was strongly controlled by rainfall. For the tropical

* Correspondence to: S. H. Mernild, Faculty of Engineering and Science, Sogn og Fjordane University College, Postboks 133, 6851 Sogndal, Norway. E-mail: sebastian.mernild@hisf.no

area of the Cordillera Blanca in Peru (9°S), glacier retreat and snow and ice meltwater result in complex hydrological interactions, where glacier retreat, according to Baraer *et al.* (2012), leads to a decrease in dry season river run-off. Accurate estimates of snow and glacial melt inputs to the hydrological budget enhance our ability to make predictions about future water resources as glaciers retreat (Gordon *et al.*, 2015).

The primary source of river run-off source in central Chile and central-western Argentina is snowmelt water (Masiokas *et al.*, 2006; Melo *et al.*, 2010). In Chile, the *Dirección General de Aguas* (DGA; http://dgasatel.mop.cl) operates more than 550 individual stream gauges (17°–54°S), covering the period from the early 1940s to the present. In the early 1940s, approximately 40 individual hydrographic stations were in operation (18°–34°S). The purpose of this monitoring network is to quantify water resource availability at economically relevant river reaches, influenced by different climate conditions along the Chilean Andes Cordillera.

Run-off time series analyses identified ongoing changes in watersheds and their suspected correlates. Rubio-Álvarez and McPhee (2010) analysed spatio-temporal variability in annual and seasonal river run-off for 44 rivers with unimpeded flow records in southern Chile (34°–45°S; 1952–2003). They suggested that decreasing run-off (37.5°–40°S) was correlated with decreasing trends in observed precipitation. Cortés *et al.* (2011) studied several rivers on the western slope of the Andes Cordillera (1961–2006; 30°–40°S), and found that hydrological changes are less apparent for rivers located at higher elevations, despite the fact that temperatures have been steadily rising in the region.

In Chile's Norte Chico region (26°–32°S), which contains some of the most glacierized basins of the region besides the Maipo and Chchapola/Tinguirrica Basins, glacier volume loss contributed 5–10% of the run-off at 3000 m above sea level (a.s.l.) (Favier *et al.*, 2009). Direct glacier run-off measurements were conducted at the snouts of four glaciers, showing that the mean annual glacier contribution to river run-off ranged between 4 and 23% – values which are greater than the glacierized fraction of the basins (Gascoin *et al.*, 2011). In addition, observations of glacier river run-off have been conducted in the Olivares Basin (33°S; 2014–2016) to understand the ratio between snow-derived run-off and basin outlet river run-off (Mernild *et al.*, 2016b).

Despite these regional studies, substantial information about the quantitative spatio-temporal hydrological conditions, including river run-off, of the numerous basins along the Andes Cordillera remains a largely unaddressed gap in our understanding. This is true for the large basins and abundant smaller basins that comprise the Cordillera. These conditions include basin outlet river run-off magnitudes, trends, and ratios between run-off and rain-derived run-off, snow-derived run-off, and ice-derived run-off. Additional coarse-scale – cross-country border – analyses can provide much needed insights into the availability of regional water resources, the terrestrial run-off impact on fjord and ocean density, stratification, and coastal circulations, and the subsequent impacts on sea-level rise and other aspects of Earth's climate system. Today, all these issues are poorly known along the Andes Cordillera and our understanding is limited. There is an urgent need for hydrological model simulations to understand the link between a changing climate and the associated changes in terrestrial freshwater run-off and oceanographic conditions along the Andes Cordillera.

In this article, SnowModel/HydroFlow (Liston and Mernild, 2012; Mernild and Liston, 2012) were used to simulate hydrological conditions along the Andes Cordillera. These simulations include freshwater river run-off magnitudes and trends, run-off routing, the spatio-temporal distribution of basin outlet river run-off to surrounding fjords and seas, and the ratios between rain-derived run-off, snow-derived run-off, and ice-derived run-off. Downscaled atmospheric reanalysis data from NASA MERRA was applied using the meteorological algorithms and sub-models implemented within MicroMet (Liston and Elder, 2006a) with a 3-h temporal resolution to simulate river run-off hydrographs and spatio-temporal river basin variability. Direct independent observed river run-off time series for the period 1979–2014 – for specific basins – were used to verify the HydroFlow simulated river hydrograph performance.

We simulated, mapped, and analysed, to our knowledge for the first time, the freshwater run-off representations for glacier, and snow-free and snow-covered land from 1979 through 2014 for the entire Andes Cordillera west of the continental divide (Figure 1). This Part IV paper focuses on: (1) linkages among run-off production from land-based liquid precipitation (rain) and snowmelt (Part I and II, Mernild *et al.*, 2016a, 2016b) and ice-melt processes (Part III, Mernild *et al.*, 2016c), and the associated spatio-temporal routing of freshwater river fluxes along the Andes Cordillera to surrounding fjords, the Pacific Ocean, and the Drake Passage; (2) latitudinal and seasonal variabilities in river run-off along the Andes Cordillera; and (3) run-off variabilities in relation to large-scale atmospheric circulation patterns. At coarsest scales, the spatio-temporal quantities of freshwater run-off and routing are associated with climactic variability ranging from Patagonian subpolar latitudes (from Tierra del Fuego) to the cold and high mountain Tropical Andes climate. At finer scales, run-off is driven by heterogeneity in the snow- and ice-covered and snow- and ice-free landscapes. To enhance our overview of run-off patterns and sources, we applied Empirical Orthogonal Function (EOF) analysis (e.g. Preisendorfer, 1998; Sparnocchia *et al.*, 2003; Mernild *et al.*, 2015) to evaluate river run-off variations; estimate contributions of rain-, snow-, and ice-based run-off; and assess correlations between ENSO (Wolter and Timlin, 2011) and the Pacific Decadal Oscillation (PDO) (Zhang *et al.*, 1997). These atmospheric circulation indices are good measures of atmospheric flow and moisture transport variability in the South Pacific (e.g. Carrasco *et al.*, 2005; Garreaud, 2009; McClung, 2013; López-Moreno *et al.*, 2014), and are important variables for terrestrial hydrosphere and

cryosphere conditions (e.g. Sagredo and Lowell, 2012; Saltzmann *et al.*, 2013; Veettil *et al.*, 2014).

2. Model description, setup, and verification

2.1. SnowModel and HydroFlow

In this research, SnowModel (Liston and Elder, 2006b) was used to characterize meteorological, snow, and glacier mass-balance processes and conditions (Parts I–III; Mernild *et al.*, 2016a, 2016b, 2016c) and the sub-model HydroFlow was applied to describe freshwater river run-off and routing processes. SnowModel is a spatially distributed meteorological, energy balance, snow, ice evolution, and freshwater run-off routing modelling system incorporating six sub-models. Here, five out of the six sub-models are used (the data assimilation sub-model, *DataAssim*, is not used): *MicroMet* is a quasi-physically-based high-resolution meteorological distribution model (Liston and Elder, 2006a), *Enbal* is an energy surface exchange and melt model (Liston, 1995; Liston *et al.*, 1999), *SnowTran-3D* is a snow surface redistribution by wind model (Liston and Sturm, 1998, 2002; Liston *et al.*, 2007), *SnowPack-ML* is a multilayer snowpack model (Liston and Mernild, 2012), and *HydroFlow* is a gridded linear-reservoir run-off routing model (Liston and Mernild, 2012; Mernild and Liston, 2012). In this system, run-off originates from rain, snowmelt that flows from the bottom of the simulated snowpack, and/or ice melt from the bare glacier surface into the supraglacial, englacial, subglacial, and subsequent the proglacial drainage system. When surface melting is simulated by SnowModel, meltwater is assumed to flow instantaneously when the surface is defined as glacier ice. When snow cover is present, the SnowPack-ML run-off routines take both internal retention and refreezing into account when snowmelts at the snowpack surface and subsequent melt water penetrates through the snowpack. Such internal snowpack routines have an effect on the run-off lag time, and how long it takes for the freshwater to reach the seas. By not including these internal snowpack routines in SnowPack-ML, it would lead to faster outflow of run-off, including an earlier initial seasonal run-off.

In HydroFlow, basins are included within a raster and adjacent cells are linked via a topographically controlled flow network (Liston and Mernild, 2012). Each grid cell acts as a linear reservoir that transfers water from itself and all upslope cells to the downslope cells within individual drainage basins, and eventually to surrounding fjords and seas. HydroFlow assumes that in each grid cell, there are two flow transfer responses: slow and fast (Liston and Mernild, 2012). Each of these transfer functions is associated with different timescales and represents the wide range of physical processes determining horizontal moisture transport through and across the domain. The slow timescale accounts for the time it takes run-off at each individual grid cell, usually produced from rain and/or snowmelt, to transport within the snow matrices (in the case of glaciers) and soil (for the case of snow-covered and snow-free land) to the routing network. Hereafter, the moisture is transported through a HydroFlow-generated routing network (the subscripts N, NE, E, SE, S, SW, W, and NW indicate the compass direction of the adjacent connecting grid box), where the fast timescale generally represents some kind of channel flow, such as that represented by supraglacial, englacial, or subglacial flow (in the case of glaciers) and river and stream channels (in the case of snow-covered and snow-free land). For each of the two flow responses, the residence time or flow velocity was estimated based on field tracer experiments (Mernild, 2006; Mernild *et al.*, 2006; Mernild *et al.*, unpublished data) and the surface slope (Liston and Mernild, 2012).

2.2. Meteorological forcing, model configuration, and simulation domain

The freshwater river run-off routing and the spatio-temporal run-off hydrograph distribution were simulated for the 35-year period from 1 April 1979 through 31 March 2014. The simulations were forced by NASA MERRA data provided on a 2/3° longitude by 1/2° latitude grid at an hourly time step (Bosilovich, 2008; Bosilovich *et al.*, 2008, 2011; Cullather and Bosilovich, 2011; Rienecker *et al.*, 2011; Robertson *et al.*, 2011). The NASA MERRA data set was aggregated to 3-h values to resolve the diurnal cycle while improving the computational efficiency (Mernild *et al.*, 2014; 2016a, Part I for further information regarding NASA MERRA forcing).

The forcing data set (NASA MERRA) strongly influences SnowModel's simulated values and biases (Liston and Hiemstra, 2011). The reanalysis data sets possess uncertainties associated with assimilated observational data sets, temporal data discontinuities, and model physics (e.g. Bosilovich *et al.*, 2008, 2011; Liston and Hiemstra, 2011). As a consequence, simulated meteorological, snow, ice mass balance, and river run-off characteristics and trends were dictated by the forcings and may be susceptible to biases associated with changes in data streams and observational inputs (for further information see Liston and Hiemstra, 2011). Substantial effort has been dedicated to producing and evaluating reanalyses, and limiting their biases, with precipitation being a key variable of interest (Bosilovich *et al.*, 2008, 2011; Cullather and Bosilovich, 2011). The relatively small number of data streams and observational inputs present during the early part of the simulations does not necessarily imply degradation in simulated meteorological fields. In the analysis that follows, we therefore assume these data increases do not significantly influence the general trends we produce and describe herein.

The NASA MERRA forcings were downscaled in MicroMet to create distributed atmospheric fields, where the spatial interpolations were performed using the Barnes objective analysis scheme, and the interpolated fields were adjusted using known temperature-elevation, wind-topography, humidity-cloudiness, and radiation-cloud-topography relationships (Liston and Elder, 2006a). Topography data for SnowModel were obtained from the United States Geological

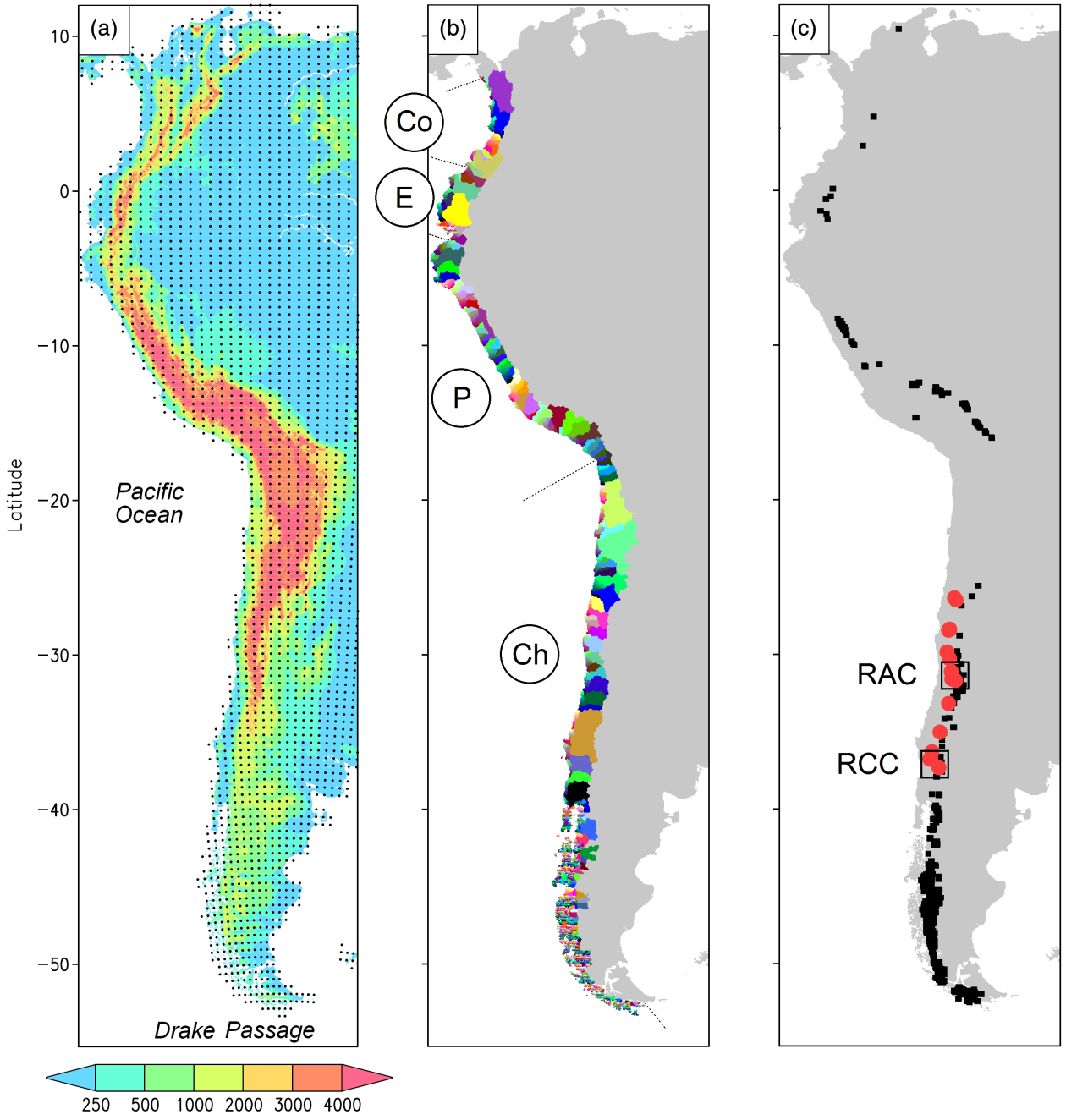

Figure 1. Western part of South America: (a) Topography (m, colour increment is not linear) and locations of MERRA atmospheric forcing grid points used in the model simulations (black dots); (b) simulated individual drainage basins (represented by multiple colours) west of the continental divide draining to the Pacific Ocean. The borders are highlighted by straight lines between the countries Colombia (Co), Ecuador (E), Peru (P), and Chile (Ch); and (c) 16 hydrometric stations (red dots) in Chile (operated by Direction General de Aguas) used for verification of simulated river run-off. Glaciers are represented by black squares (added 20 km to the edges of each glacier to make them more visible in the figure). Also, two specific regions are illustrated from where examples of basin run-off and hydrographs are illustrated (see bold square): RAC and RCC. [Colour figure can be viewed at wileyonlinelibrary.com].

Survey's 7.5 arc-second Global Multi-resolution Terrain Elevation Data 2010 (GMTED2010; Danielson and Gesch, 2011), and rescaled to a 4-km horizontal grid increment. The land cover distribution file was a hybrid data set created from a 2009 300-m Global Land Cover (GlobCover 2.3, http://ionia1.esrin.esa.int/) for non-glacier areas and from the Randolph Glacier Inventory v. 4.0 for glaciers (Pfeffer *et al.*, 2014). Regarding changes in glacier area, hypsometry, and thinning, SnowModel neglects these influences throughout the simulation period. Instead, SnowModel uses a constant glacier area and elevation defined from data sets produced during the 2000s and 2010, respectively (Mernild *et al.*, 2016c). The use of these constant conditions may result in errors in the simulated surface mass balances (SMB) budget and run-off, particularly at the beginning of the simulation period. Also, it may neglect a decrease in dry season river run-off as observed in Cordillera Blanca in Peru (9°S) (Baraer *et al.*, 2012), since

Table 1. Example of statistical information regarding daily simulated run-off and observed run-off from 16 hydrometric stations and the two individual hydrometric stations: RCC and RAC. The brackets indicate how much simulated run-off is overestimated compared to observed run-off.

	Sixteen hydrometric stations		RCC		RAC	
	Simulated run-off	Observed run-off	Simulated run-off	Observed run-off	Simulated run-off	Observed run-off
Average ($\times 10^7$ m^3)	0.33 (13%)	0.29	1.21 (3%)	1.17	0.32 (9%)	0.29
Standard deviation ($\times 10^7$ m^3)	0.56	0.58	1.02	1.14	0.35	0.28
r^2	0.52		0.60		0.69	
r^2 range	0.31–0.71		–		–	

glacier area retreat is not accounted for throughout the simulation period.

HydroFlow divided the domain into individual drainage basins (Figure 1(b)), each with its own streamflow network that drains run-off to downslope areas and into the adjacent fjords and seas. For the domain west of the continental divide, HydroFlow generated 4224 individual basins all draining into fjords connected to The Pacific Ocean or The Drake Passage, or directly into the Pacific Ocean or The Drake Passage (Figure 1(a)). The individual HydroFlow estimated basins varied in size from 32 to 62 864 km^2 (located near Concepción, Chile; 37°S), with a mean and median basin size of 294 and 48 km^2, respectively, where 83% of the drainage basins cover equal to or less than 100 km^2. These many relatively small basins (<100 km^2) cover 14% of the total drainage area, where about two thirds of these basins are located south of the city Puerto Montt (41°S), Chile.

2.3. SnowModel and HydroFlow verification

This article is the fourth in a series of papers about SnowModel MERRA simulations for the Andes Cordillera on climate, snow, glacier mass balance, and hydrological conditions, including river run-off routing. The simulations presented were verified against independent observational data sets. In Part I (Mernild *et al.*, 2016a), SnowModel-simulated maximum annual snow cover extent, snow depths, and snow density were evaluated against a suite of remote sensing and field observations. The MODIS/Terra Snow Cover Daily L3 Global 500-m grid (MOD10A1) product (Hall *et al.*, 1995, 2006; Hall and Riggs, 2007) was used from 2000/2001 through 2013/2014 for validation of maximum annual simulated snow cover extent for a rectangle between 31.5°–40.0°S and 69.2°–72.3°W, indicating acceptable results (for detailed information about the quantitative model skill metrics, see Mernild *et al.*, 2016a). Additionally, more than 3000 individual observed snow depths and snow densities measured between 30° and 37°S for the central Chilean Andes Cordillera (Ayala *et al.*, 2014; Cornwell *et al.*, 2016) were used. These observations cover the period 2010 through 2014 and were recalculated into mean 4-km grid increments identical to the grids used in SnowModel and used for verification of SnowModel grid simulated snow depths and snow densities. Acceptable verification was determined according to the deviation between simulated and observed mean grid snow depth values.

In Part II, for a specific drainage basin – the Olivares Basin (33°S; 548 km^2) – simulated snow cover extent for specific dates, snow line (the snow line is a net product of seasonal accumulation and ablation processes), snow depletion curves, and freshwater run-off for the period 1979–2014 were verified against independent observations, yielding satisfactory results (for detailed information about the quantitative model skill metrics, see Mernild *et al.*, 2016b).

In Part III, simulated glacier SMB time series (1979–2012) were verified against independent direct observed annual glacier SMB time series from seven glaciers (e.g. WGMS, 2013; Mernild *et al.*, 2015), having a total of 72 direct observed annual glacier SMB; the seven glaciers are ≥1 km^2, equal to the grid increment size used for the glacier SMB simulations. In addition, these simulations were compared with satellite gravimetry and altimetry-derived SMB (Gardner *et al.*, 2013). For the independent SMB data sets, the verification indicated a good agreement between simulations and independent observations (for detailed information about the quantitative model skill metrics, see Mernild *et al.*, 2016c).

SnowModel simulated river run-off values were verified against coincident independently observed river run-off from DGA hydrographic stations in central Chile (28°–39°S) (in this article). DGA observed river run-off time series values spanning ≥98% of the 1979–2014 simulation range were chosen for model verification, resulting in 16 comparison pairs covering the latitudes 25°–40°S (Figure 1(c) and Table 1). As examples, two hydrographic stations, one located at Rio Aconcagua en Chacabuquito (RAC; 30°S) and another at Rio Cautin en Cajon (RCC; 37°S) are illustrated in Figure 2, together with the HydroFlow topographically controlled flow network for the basins. Daily simulated and observed run-off from all 16 selected hydrographic stations (Figure 3(a)) shows on average an r^2 value = 0.51, $p < 0.01$ (where r^2 is the explained variance and p is the level of significance) and a r^2 range from 0.31 to 0.71. It indicates that HydroFlow overall was able to account for 51% of the variance in river run-off at all of the 16 selected hydrographic stations (Table 1). For example, for the stations RAC and RCC the r^2 values were 0.60 ($p < 0.01$) and 0.69 ($p < 0.01$) (Table 1), respectively. Furthermore,

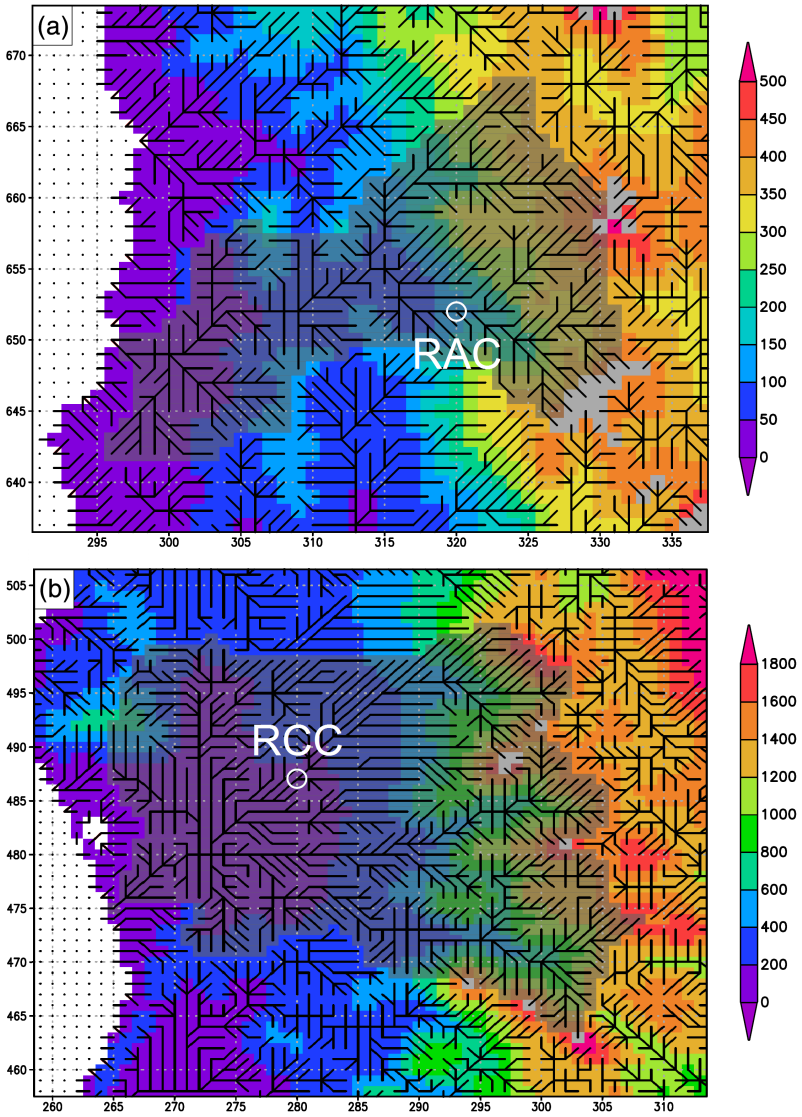

Figure 2. Examples of flow networks calculated from gridded topography and ocean-mask data sets to illustrate the HydroFlow network configuration over the simulation domain for the basins including (a) the RAC hydrographic station and (b) the RCC hydrological station. The hydrological stations are marked with a white circle, the flow network with black lines, and the basin with a transparent shaded grey of which drains into the ocean (white colour). Glaciers are represented by light grey squares and topography by multiple colours. [Colour figure can be viewed at wileyonlinelibrary.com].

we did a Nash–Sutcliffe coefficient (NSC) test (Nash and Sutcliffe, 1970) for the 16 selected hydrographic stations, with a mean NSC value of 0.47 and a range from 0.35 to 0.64. If the NSC is 1, then the model is a perfect fit to the observations. If NSC is less than 1, decreasing values represent a decline in goodness of fit, where zero and negative values represent major deviations between the modelled and observed data and the observed mean is a better predictor than the model. In Figures 3(b) and (c), the simulated and observed hydrograph time series (based on daily values) are shown for both RAC and RCC, indicating similarity between seasonal (intra-annual) variations in simulated and observed river run-off at the two hydrographic stations RAC and RCC (Figure 3(c)). Overall, the highlighted run-off verifications provide confidence in the simulated run-off time series for the selected hydrometric stations (located approximately between 25° and 40°S; Figure 1(c)). Similar confidence in simulated run-off was illustrated by Beamer *et al.* (2016) when using SnowModel and HydroFlow for Gulf of Alaska drainage basins.

3. EOF analysis

We applied EOF analysis to characterize spatio-temporal pattern in run-off and water source. EOF is a tool that ordinates the spatial and temporal data to find combinations of locations that vary consistently through time and combinations of time that vary in a spatially consistent manner. More specifically, the first few major axes of the EOF analysis explain variations in river run-off through both time and space. Eigenvectors associated with such an analysis are linked to spatial locations and reveal the influence of different geographic locations on the summarized run-off patterns and allow further analyses of large-scale atmospheric-ocean covariates linked to the

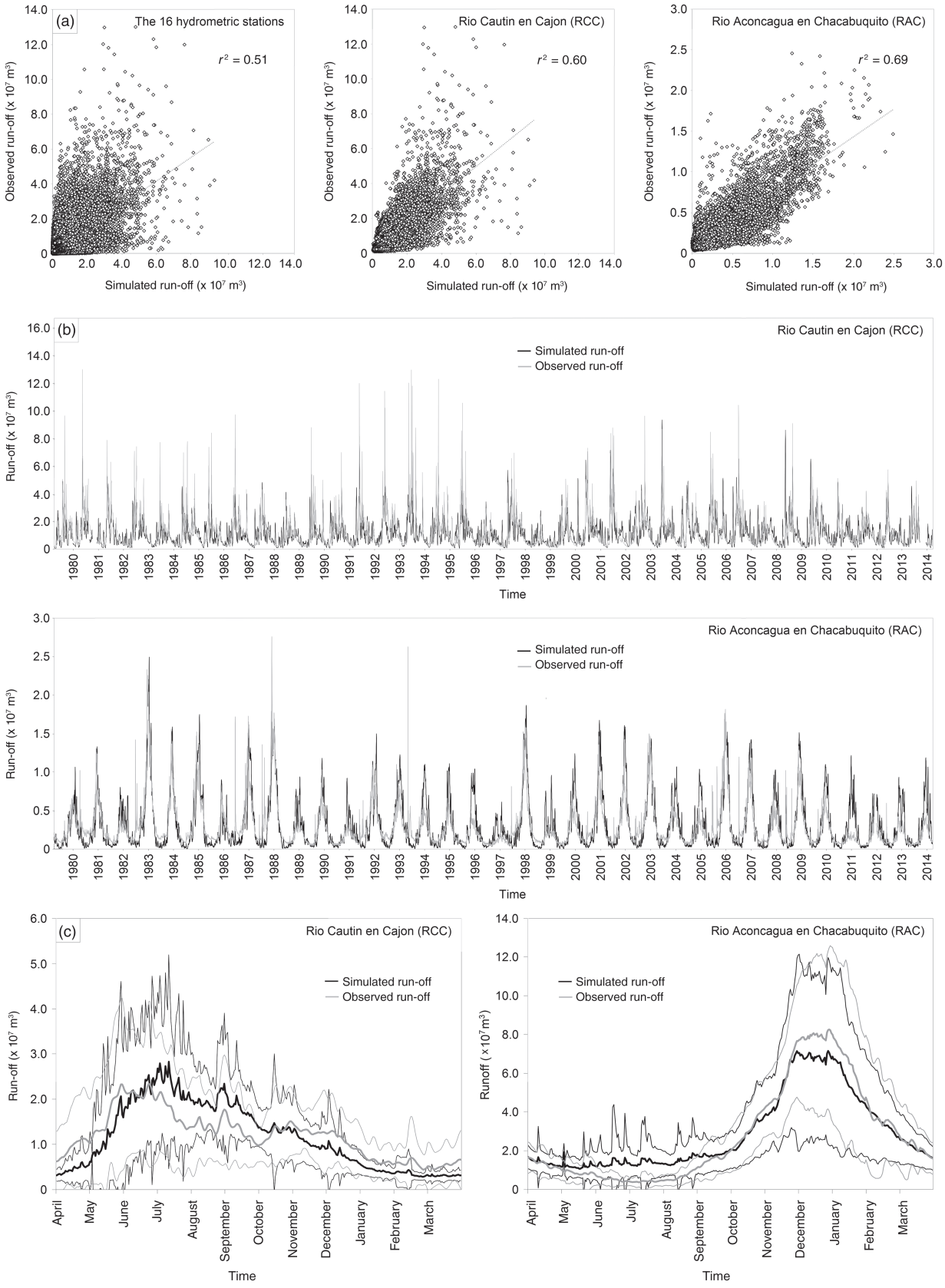

Figure 3. (a) A comparison between daily simulated run-off and observed run-off for 16 hydrometric stations and an example of two of the individual stations RCC and RAC (1 April 1979 through 31 March 2014); (b) daily simulated and observed run-off time series from RCC and RAC; (c) mean seasonal hydrographs (bold lines) 1979–2014 including time series of one standard deviation (thin lines) for the two individual stations RCC and RAC.

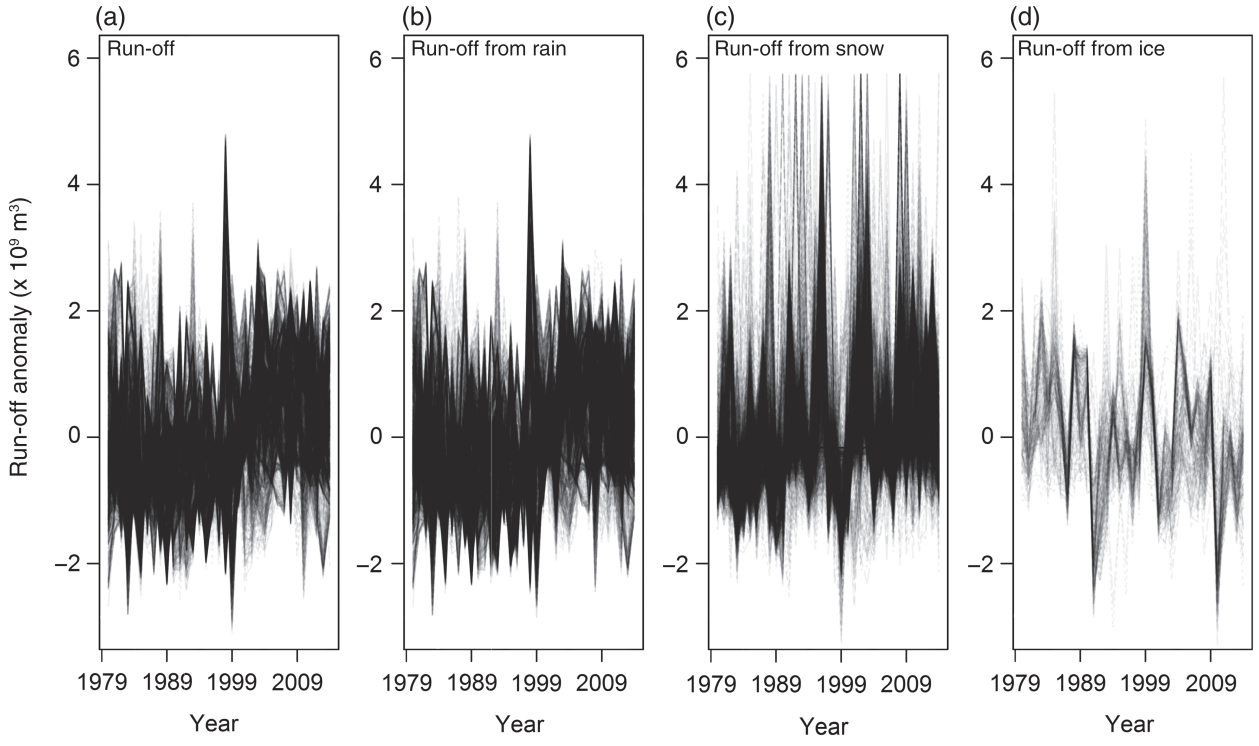

Figure 4. Time series of simulated annual run-off anomaly from each individual drainage basin west of the continental divide for the period 1979–2014: (a) total run-off, (b) run-off from rain, (c) run-off from snowmelt, and (d) run-off from ice melt.

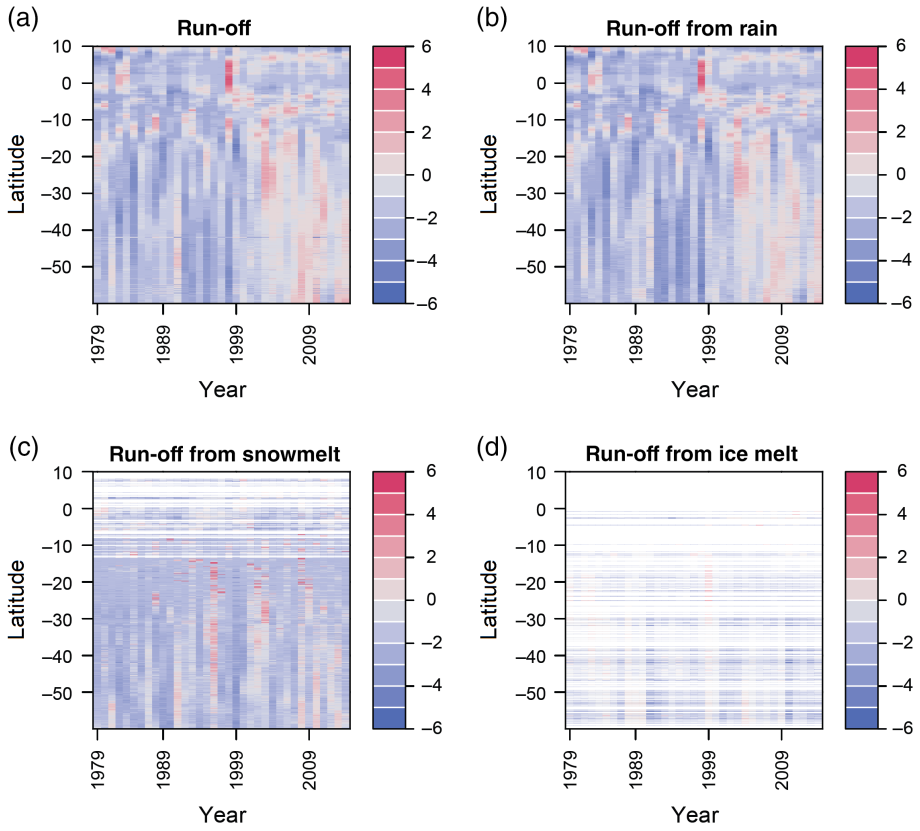

Figure 5. A 'field' representation of the scaled and centred, simulated run-off data indexed by latitude and year (1979–2014): (a) total run-off, (b) run-off from rain, (c) run-off from snowmelt, and (d) run-off from ice melt. The scale bar indicates run-off values above and below average (e.g. the data were centred at 0). [Colour figure can be viewed at wileyonlinelibrary.com].

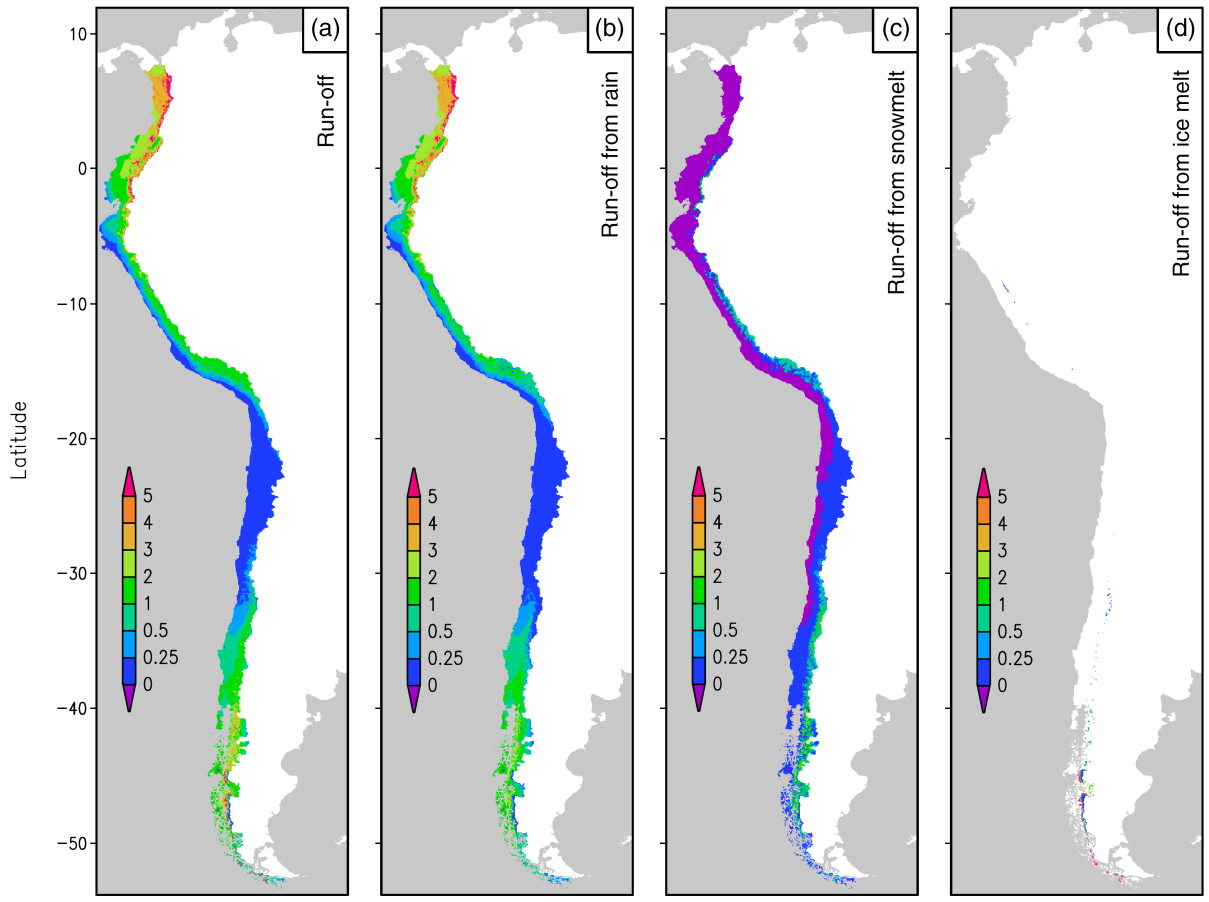

Figure 6. Simulated 35-year average run-off in each grid cell west of the continental divide (m w.e., colour increment is not linear): (a) total annual run-off, (b) annual run-off from rain, (c) annual run-off from snowmelt, and (d) annual run-off from ice melt. [Colour figure can be viewed at wileyonlinelibrary.com].

EOFs. In addition, the temporally summarized spatial data can be explored with cross-correlation analysis between the run-off patterns and larger-scale atmospheric climate indices such as ENSO and PDO.

We applied EOF to total run-off (henceforth mentioned as run-off), rain-derived run-off, snowmelt-derived run-off, and ice melt-derived run-off (in Figure 4 the time series of simulated annual run-off anomaly from each individual drainage basin west of the continental divide for the period 1979–2014 is shown). Figure 5 provides a 'field' representation of the spatio-temporal pattern in basin annual run-off for rain, snow, ice, and the combined total, with latitude on the *y*-axis and time on the *x*-axis and colours indicating the spatio-temporal patterns. We specifically examined the eigenvectors of the first two EOFs (EOF1–2) to gain insight into the correlation between temporal trends and spatial locations. We also examined how the first two EOFs (temporal component) vary with two large-scale atmospheric-ocean indices: the multivariate ENSO Index obtained from Wolter and Timlin (2011) and the PDO obtained from Zhang *et al.* (1997). We used cross-correlation analyses for this, which allow insight into whether the run-off patterns are linked to ENSO and PDO as they occur or with a lag, where signals of ENSO or PDO show in the run-off patterns years after the events.

ENSO is comprised of different physical parameters observed across the tropical Pacific Ocean, such as sea-level pressure, surface air temperature, sea surface temperature, cloud fraction, and the zonal and meridional components of the surface wind. Normalized positive ENSO values represent El Niño events and negative values La Niña events (Wolter and Timlin, 2011). The PDO reflects climate variability in the Pacific Ocean, but over a longer timescale than the ENSO. The ENSO cycles typically remain in the same phase for 6–18 months, where the PDO may remain in the same phase for one to two decades. The PDO consists of cold (negative) and warm (positive) phases, defined by ocean sea surface temperature anomalies in the northeast and tropical Pacific Ocean. These anomalies are implicated in upper level atmospheric winds causing droughts, and affect land surface temperatures around the Pacific. When normalized sea surface temperatures are anomalously cold for the central North Pacific and relatively warm near the equator and along the Pacific Coast of South America (and when standardized sea-level pressure is below average over the North Pacific), the PDO has a positive phase, and vice versa for the negative phase (e.g. Zhang *et al.*, 1997). Importantly, if ENSO and PDO are in the same phase, impacts from El Niño and La Niña are likely reinforced,

Table 2. Simulated annual mean run-off and standard deviation (standard deviation is presented for the 35-year mean period) for the four countries Colombia, Ecuador, Peru, and Chile from 1979 through 2014, and on pentadal scale. The linear trends in run-off are highlighted in brackets.

	Parameters (m^3)	Colombia	Ecuador	Peru	Chile[a]	Total (domain)
1979/1980–1983/1984	Run-off	38.0×10^{10}	16.6×10^{10}	24.5×10^{10}	50.3×10^{10}	129.4×10^{10}
	Run-off from rain	37.8×10^{10} (99%)	16.1×10^{10} (97%)	21.0×10^{10} (86%)	35.2×10^{10} (70%)	111.2×10^{10} (86%)
	Run-off from snowmelt	0.1×10^{10} (<1%)	0.5×10^{10} (3%)	3.5×10^{10} (14%)	11.1×10^{10} (22%)	15.2×10^{10} (12%)
	Run-off from ice melt	0.1×10^{10} (<1%)	$<0.1\times10^{10}$ (<1%)	$<0.1\times10^{10}$ (<1%)	4.0×10^{10} (8%)	3.0×10^{10} (2%)
	Run-off from non-glacierized areas	38.0×10^{10} (>99%)	16.6×10^{10} (>99%)	24.5×10^{10} (>99%)	43.3×10^{10} (86%)	122.4×10^{10} (95%)
	Run-off from glacierized areas	$<0.1\times10^{10}$ (<1%)	$<0.1\times10^{10}$ (<1%)	$<0.1\times10^{10}$ (<1%)	7.0×10^{10} (14%)	7.0×10^{10} (5%)
1984/1985–1988/1989	Run-off	37.8×10^{10}	15.3×10^{10}	22.7×10^{10}	48.9×10^{10}	124.7×10^{10}
	Run-off from rain	37.6×10^{10} (99%)	14.7×10^{10} (96%)	19.2×10^{10} (85%)	33.5×10^{10} (69%)	105.2×10^{10} (84%)
	Run-off from snowmelt	0.1×10^{10} (<1%)	0.6×10^{10} (4%)	3.5×10^{10} (15%)	11.5×10^{10} (24%)	15.7×10^{10} (13%)
	Run-off from ice melt	0.1×10^{10} (<1%)	$<0.1\times10^{10}$ (<1%)	$<0.1\times10^{10}$ (<1%)	3.9×10^{10} (7%)	3.8×10^{10} (3%)
	Run-off from non-glacierized areas	37.8×10^{10} (>99%)	15.3×10^{10} (>99%)	22.7×10^{10} (>99%)	42.1×10^{10} (86%)	117.9×10^{10} (95%)
	Run-off from glacierized areas	$<0.1\times10^{10}$ (<1%)	$<0.1\times10^{10}$ (<1%)	$<0.1\times10^{10}$ (<1%)	6.8×10^{10} (14%)	6.8×10^{10} (5%)
1989/1990–1993/1994	Run-off	3.5×10^{11}	15.8×10^{10}	22.6×10^{10}	49.5×10^{10}	123.0×10^{10}
	Run-off from rain	3.5×10^{11} (99%)	15.2×10^{10} (96%)	19.3×10^{10} (85%)	34.0×10^{10} (69%)	103.5×10^{10} (84%)
	Run-off from snowmelt	0.1×10^{10} (<1%)	0.6×10^{10} (4%)	3.3×10^{10} (15%)	12.1×10^{10} (24%)	16.1×10^{10} (13%)
	Run-off from ice melt	0.1×10^{10} (<1%)	$<0.1\times10^{10}$ (<1%)	$<0.1\times10^{10}$ (<1%)	3.4×10^{10} (7%)	3.4×10^{10} (3%)
	Run-off from non-glacierized areas	3.5×10^{11} (>99%)	15.8×10^{10} (>99%)	22.6×10^{10} (>99%)	43.1×10^{10} (87%)	116.6×10^{10} (95%)
	Run-off from glacierized areas	$<0.1\times10^{10}$ (<1%)	$<0.1\times10^{10}$ (<1%)	$<0.1\times10^{10}$ (<1%)	6.4×10^{10} (13%)	6.4×10^{10} (5%)
1994/1995–1998/1999	Run-off	39.4×10^{10}	21.2×10^{10}	25.4×10^{10}	48.2×10^{10}	134.2×10^{10}
	Run-off from rain	39.3×10^{10} (99%)	20.7×10^{10} (98%)	22.0×10^{10} (87%)	33.1×10^{10} (69%)	115.1×10^{10} (86%)
	Run-off from snowmelt	0.1×10^{10} (<1%)	0.5×10^{10} (2%)	3.4×10^{10} (13%)	11.3×10^{10} (23%)	15.3×10^{10} (12%)
	Run-off from ice melt	$<0.1\times10^{10}$ (<1%)	$<0.1\times10^{10}$ (<1%)	$<0.1\times10^{10}$ (<1%)	3.8×10^{10} (8%)	3.8×10^{10} (2%)
	Run-off from non-glacierized areas	39.4×10^{10} (>99%)	21.2×10^{10} (>99%)	25.4×10^{10} (>99%)	41.6×10^{10} (86%)	127.6×10^{10} (95%)
	Run-off from glacierized areas	$<0.1\times10^{10}$ (<1%)	$<0.1\times10^{10}$ (<1%)	$<0.1\times10^{10}$ (<1%)	6.6×10^{10} (14%)	6.6×10^{10} (5%)
1999/2000–2003/2004	Run-off	43.3×10^{10}	25.4×10^{10}	21.8×10^{10}	54.4×10^{10}	144.9×10^{10}
	Run-off from rain	43.1×10^{10} (99%)	24.7×10^{10} (97%)	19.0×10^{10} (87%)	37.6×10^{10} (69%)	124.5×10^{10} (86%)
	Run-off from snowmelt	0.1×10^{10} (<1%)	0.6×10^{10} (2%)	2.8×10^{10} (13%)	13.5×10^{10} (25%)	16.9×10^{10} (12%)
	Run-off from ice melt	0.1×10^{10} (<1%)	0.1×10^{10} (1%)	$<0.1\times10^{10}$ (<1%)	3.3×10^{10} (6%)	3.5×10^{10} (2%)
	Run-off from non-glacierized areas	43.3×10^{10} (>99%)	25.4×10^{10} (>99%)	21.8×10^{10} (>99%)	48.1×10^{10} (88%)	138.5×10^{10} (96%)
	Run-off from glacierized areas	$<0.1\times10^{10}$ (<1%)	$<0.1\times10^{10}$ (<1%)	$<0.1\times10^{10}$ (<1%)	6.3×10^{10} (12%)	6.4×10^{10} (4%)
2004/2005–2008/2009	Run-off	45.5×10^{10}	26.6×10^{10}	22.5×10^{10}	55.8×10^{10}	150.4×10^{10}
	Run-off from rain	45.4×10^{10} (99%)	26.0×10^{10} (98%)	19.6×10^{10} (87%)	38.7×10^{10} (69%)	129.8×10^{10} (86%)
	Run-off from snowmelt	0.1×10^{10} (<1%)	0.6×10^{10} (2%)	2.9×10^{10} (13%)	13.3×10^{10} (24%)	16.9×10^{10} (11%)
	Run-off from ice melt	$<0.1\times10^{10}$ (<1%)	$<0.1\times10^{10}$ (<1%)	$<0.1\times10^{10}$ (<1%)	3.8×10^{10} (7%)	3.7×10^{10} (3%)
	Run-off from non-glacierized areas	45.5×10^{10} (>99%)	26.6×10^{10} (>99%)	22.5×10^{10} (>99%)	48.6×10^{10} (87%)	143.3×10^{10} (95%)
	Run-off from glacierized areas	$<0.1\times10^{10}$ (<1%)	$<0.1\times10^{10}$ (<1%)	$<0.1\times10^{10}$ (<1%)	7.2×10^{10} (13%)	7.1×10^{10} (4%)
2009/2010–2013/2014	Run-off	47.5×10^{10}	26.3×10^{10}	23.1×10^{10}	52.0×10^{10}	148.9×10^{10}
	Run-off from rain	47.4×10^{10} (99%)	25.7×10^{10} (98%)	19.9×10^{10} (86%)	36.2×10^{10} (70%)	129.3×10^{10} (87%)
	Run-off from snowmelt	0.1×10^{10} (<1%)	0.6×10^{10} (2%)	3.2×10^{10} (14%)	12.6×10^{10} (24%)	16.5×10^{10} (11%)

Table 2. continued

	Parameters (m^3)	Colombia	Ecuador	Peru	Chile[a]	Total (domain)
	Run-off from ice melt	$<0.1\times10^{10}$ (<1%)	$<0.1\times10^{10}$ (<1%)	$<0.1\times10^{10}$ (<1%)	3.2×10^{10} (6%)	3.1×10^{10} (2%)
	Run-off from non-glacierized areas	47.5×10^{10} (>99%)	26.3×10^{10} (>99%)	23.1×10^{10} (>99%)	45.7×10^{10} (88%)	142.5×10^{10} (96%)
	Run-off from glacierized areas	$<0.1\times10^{10}$ (<1%)	$<0.1\times10^{10}$ (<1%)	$<0.1\times10^{10}$ (<1%)	6.3×10^{10} (12%)	6.4×10^{10} (4%)
1979/1980–2013/2014	Run-off	$40.9\pm5.60\times10^{10}$ (30%) (0.37×10^{10} m^3 $year^{-1}$)	$21.0\pm5.63\times10^{10}$ (15%) (0.43×10^{10} m^3 $year^{-1}$)	$23.3\pm2.58\times10^{10}$ (17%) (-0.03×10^{10} m^3 $year^{-1}$)	$51.3\pm4.09\times10^{10}$ (38%) (0.17×10^{10} m^3 $year^{-1}$)	$136.5\pm12.15\times10^{10}$ (0.94×10^{10} m^3 $year^{-1}$)
	Run-off from rain	40.8×10^{10} (99%) (0.37×10^{10} m^3 $year^{-1}$)	20.4×10^{10} (97%) (0.43×10^{10} m^3 $year^{-1}$)	20.0×10^{10} (86%) (-0.02×10^{10} m^3 $year^{-1}$)	35.5×10^{10} (69%) (0.12×10^{10} m^3 $year^{-1}$)	116.9×10^{10} (86%) (0.88×10^{10} m^3 $year^{-1}$)
	Run-off from snowmelt	0.1×10^{10} (<1%) ($<0.01\times10^{10}$ m^3 $year^{-1}$)	0.6×10^{10} (3%) ($<0.01\times10^{10}$ m^3 $year^{-1}$)	3.2×10^{10} (14%) (-0.01×10^{10} m^3 $year^{-1}$)	12.2×10^{10} (24%) (0.07×10^{10} m^3 $year^{-1}$)	16.1×10^{10} (12%) (0.05×10^{10} m^3 $year^{-1}$)
	Run-off from ice melt	$<0.1\times10^{10}$ (<1%) ($<0.01\times10^{10}$ m^3 $year^{-1}$)	$<0.1\times10^{10}$ (<1%) ($<0.01\times10^{10}$ m^3 $year^{-1}$)	0.1×10^{10} (<1%) ($<0.01\times10^{10}$ m^3 $year^{-1}$)	3.6×10^{10} (7%) (-0.02×10^{10} m^3 $year^{-1}$)	3.5×10^{10} (2%) (0.01×10^{10} m^3 $year^{-1}$)
	Run-off from non-glacierized areas	40.9×10^{10} (>99%)	21.0×10^{10} (>99%)	23.3×10^{10} (>99%)	44.6×10^{10} (87%)	129.8×10^{10} (95%)
	Run-off from glacierized areas	$<0.1\times10^{10}$ (<1%)	$<0.1\times10^{10}$ (<1%)	$<0.1\times10^{10}$ (<1%)	6.7×10^{10} (13%)	6.7×10^{10} (5%)

[a]For Chile, it is only the run-off draining into the Pacific Ocean and the Drake Passage.

and vice versa when they are out of phase (e.g. Yuan and Martinson, 2000, 2001).

4. Results and discussion

4.1. Grid run-off distribution

SnowModel gridded 35-year (1979–2014) mean run-off and its rain-, snowmelt-, and ice melt-derived components for the Andes Cordillera west of the continental divide show highest run-off values for northern and southern parts of the domain (Figures 6(a)–(d)). Colombia and northern Ecuador (6°N–6°S), and Patagonia (38°–45°S) estimates were greater than 5-m water equivalent (w.e.). High values were expected for Patagonia, which is chronically impacted by severe subpolar low-pressure systems and their attendant high precipitation rates (e.g. Romero, 1985; Paruelo *et al.*, 1998; Garreaud *et al.*, 2009). The lowest run-off values (<0.25-m w.e.) were obtained along the coastal zone of Peru and between the Atacama Desert (18°–20°S) and Santiago de Chile (33°S), showing distinct regional-scale grid run-off variability throughout the simulation domain.

For the domain, the simulated 35-year mean run-off was $136.5\pm12.2\times10^{10}\,m^3$ (where $\pm$ means one standard deviation; Table 2), distributed among Colombia ($40.9\pm5.6\times10^{10}\,m^3$), Ecuador ($21.0\pm5.6\times10^{10}\,m^3$), Peru ($23.3\pm2.6\times10^{10}\,m^3$), and Chile ($51.3\pm4.1\times10^{10}\,m^3$) (Table 2). This indicates that for the 35-year period, Colombia accounted for 30%, Ecuador 15%, Peru 17%, and Chile 38% of the domain's run-off (Table 2).

The gridded 35-year mean run-off correlates highly with the gridded 35-year mean rain-based run-off (Figure 6), where for the entire domain 86%, or $116.9\times10^{10}\,m^3$, of the run-off originated from rain (Table 2). This emphasizes that run-off, on average for the domain, is highly influenced by a pluvial regime. In particular, the northern part of the domain was controlled by rain-derived run-off, accounting for 99% of the run-off from Colombia, Ecuador 97%, Peru 86%, and Chile 69% (Table 2). Crespo *et al.* (2011) used observations to confirm this pluvial regime for 13 monitored micro-basins in the Andes of southern Ecuador (4°S), where run-off was strongly controlled by annual rainfall. Similar conclusions were stated by Rubio-Álvarez and McPhee (2010) for southern Chile, where a decrease in run-off corresponded with decreasing trends in observed precipitation. Therefore, along the Andes Cordillera, the variability in run-off was influenced by the meteorological conditions, including the north–south temperature gradient – going towards relatively lower mean annual air temperatures in the south in Patagonia (subpolar climate), compared to the north (tropical climate) (Mernild *et al.*, 2016a) – together with the presence of increasing snow and glacier coverage towards Patagonia to the south.

Snowmelt-derived run-off (Figure 6(c)) over 35 years is spatially tied to snow duration in the high Andes mountains and in Patagonia (for a detailed spatio-temporal

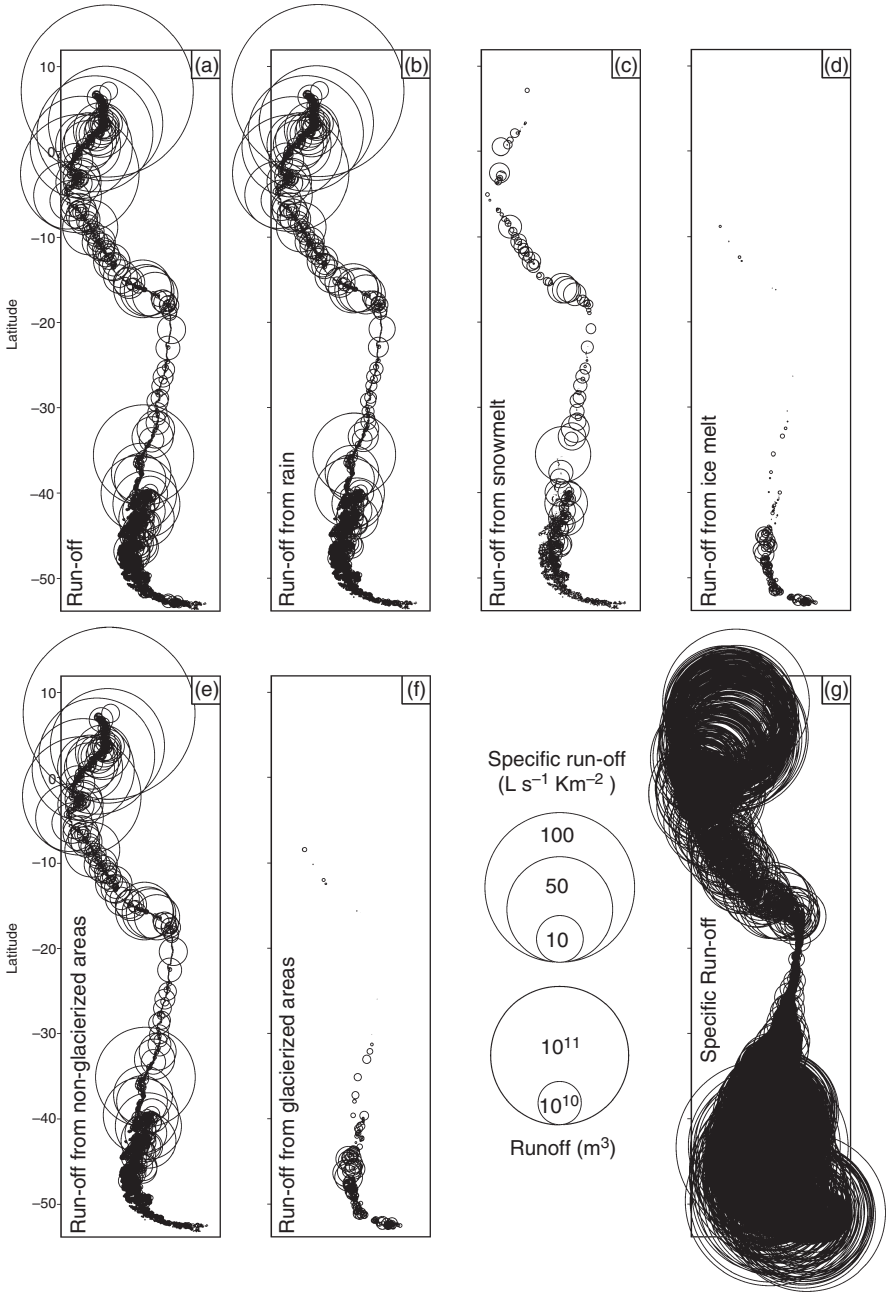

Figure 7. Simulated 35-year average annual run-off from each individual drainage basins west of the continental divide (the area of each circle is proportional to the run-off): (a) total run-off, (b) run-off from rain, (c) run-off from snowmelt, (d) run-off from ice melt, (e) run-off from non-glacierized areas, (f) run-off from glacierized areas, and (g) specific run-off.

description of snow conditions in the Andes Cordillera, see Mernild *et al.*, 2016a). Snowmelt run-off averaged <1% for Colombia, Ecuador (3%), Peru (14%), and Chile (24%) (Table 2). For Chile, snowmelt run-off contributions averaged higher than for any of the three countries within the domain (Colombia, Ecuador, and Peru), emphasizing a higher degree of nival run-off, where the maximum basin values of snowmelt-based run-off was ∼60% for central Chile and ∼80% for Patagonia. Similar conditions are confirmed by, e.g., Masiokas *et al.* (2006), Favier *et al.* (2009), Melo *et al.* (2010), and Mernild *et al.* (2016b), where snowpack and snowmelt changes on the individual basin scale in central Chile, central-western Argentina, and Norte Chico region were the primary source for run-off, annual variability, and water budget.

Ice melt-derived run-off (Figure 6(d)) is scattered along the Andes Cordillera. The ratio between ice melt base run-off and run-off is <1% for Colombia, Ecuador, and Peru and 7% for Chile (Table 2), associated with the increasing ice coverage towards the south. Owing to ongoing temporal changes in ice coverage for South America, where glaciers have retreated and thinned in response to climate changes since the end of the Little Ice Age (e.g. Masiokas *et al.*, 2006; Le Quesne *et al.*, 2009; Malmros *et al.*, 2016), it is expected that the ratio between ice melt-derived run-off and total run-off will decrease

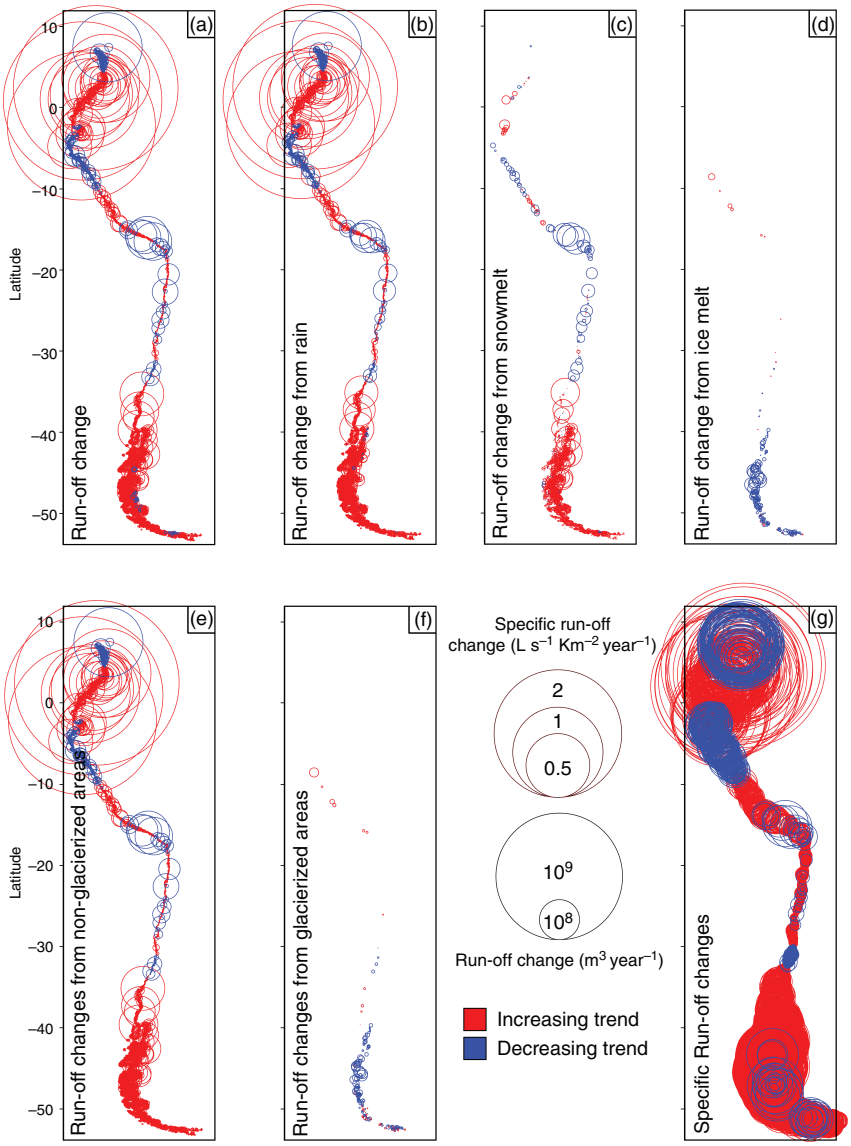

Figure 8. Simulated 35-year annual changes in run-off from each individual drainage basins west of the continental divide (the area of each circle is proportional to the run-off): (a) total run-off change, (b) run-off change from rain, (c) run-off change from snowmelt, (d) run-off change from glacier ice melt, (e) run-off change from non-glacierized areas, (f) run-off change from glacierized areas, and (g) specific run-off change. [Colour figure can be viewed at wileyonlinelibrary.com].

because the annual ice melt-derived run-off will decline as reductions in glacier area outweigh the effect of glacier melting (AMAP, 2011).

Overall, for the domain, 95% of the simulated run-off originated from non-glacierized basins and 5% from glacierized basins (Table 2), highlighting that rain-derived run-off from non-glacierized basins is the greatest contributor to run-off west of the continental watershed divide. For the 35-year period, Colombia, Ecuador, and Peru, >99% of the river run-off was from non-glacierized basins, and <1% was from glacierized basins; for Chile, it was 87 and 13%, respectively (Table 2). On pentadal scales (1979/1980–1983/1984, 1984/1985–1988/1989, etc.), the ratios between simulated mean run-off from non-glacierized and glacierized areas are not significantly different compared to the mean ratio for the 35-year period. The same insignificant differences in ratios occurred between run-off and rain, run-off and snowmelt, and run-off and ice melt between pentadal mean values and the 35-year mean value, even though run-off for the domain changed by 0.94×10^{10} m^3 year^{-1} (significant; $p < 0.01$) for the simulation period (Table 2). When analysed by specific countries, run-off changed by 0.43×10^{10} m^3 year^{-1} for Ecuador (significant; $p < 0.01$), 0.37×10^{10} m^3 year^{-1} for Colombia (significant; $p < 0.01$), 0.17×10^{10} m^3 year^{-1} for Chile (insignificant), and 0.03×10^{10} m^3 year^{-1} for Peru (insignificant) over the 35-year period (Table 2).

4.2. Spatial distribution of basin run-off

In Figures 7 and 8, SnowModel-simulated 35-year mean river run-off is shown together with run-off trends from each individual drainage basin outlet west of the continental divide. The figures include rain-derived run-off,

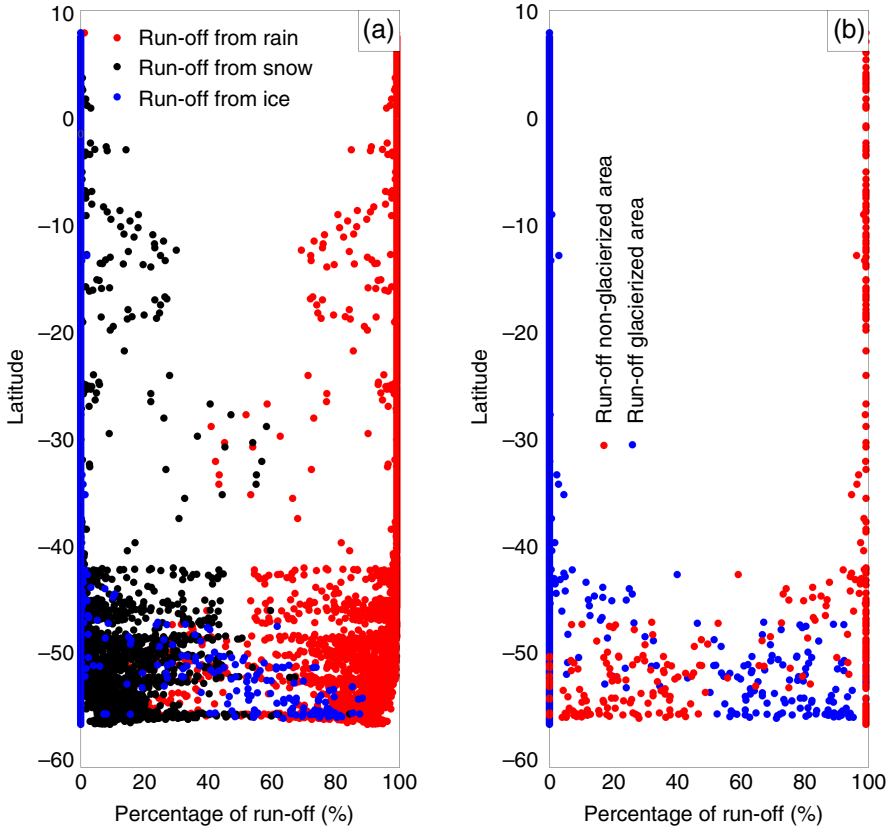

Figure 9. The percentage of seasonal basin run-off versus latitude for (a) run-off from rain, snowmelt, and ice melt and (b) run-off from non-glacierized areas and glacierized areas. [Colour figure can be viewed at wileyonlinelibrary.com].

snowmelt-derived run-off, and ice melt-derived run-off, run-off from non-glacierized areas, glacierized areas, and specific run-off (run-off volume per unit drainage area per time, $L\,s^{-1}\,km^{-2}$). In Figures 7(a)–(f), variability in the 35-year mean run-off between neighbouring basins occurred (these run-off variations are expected to be useful for future studies linking these run-off to coastal circulations to understand the linkages between terrestrial and marine environments). It is reasonable to believe that the differences in mean basin run-off regimes between pluvial, nival, and glacionival are related to geographical locations and differences in basin characteristics (e.g. size and hypsometry), snow coverage, ice coverage, and climate forcing functions. For example, the Andes Cordillera acts as a topographic barrier enhancing the terrestrial precipitation on the western sides (e.g. Mernild *et al.*, 2016a), contributing to the pluvial regimen in river run-off. High 35-year mean basin river outlet run-off (maximum: $7.3 \pm 1.9 \times 10^{10}\,m^3$; 2°S) and high linear run-off trends (maximum: $0.2 \times 10^{10}\,m^3\,year^{-1}$; 2°N) occurred in the northern part of the domain in Colombia and Ecuador and in the lower half of the domain, especially around the Lake District of Chile (39°–41°S) (Figures 7(a) and 8(a)) [linear spatial run-off trends (Figure 8) which are not significantly different from the normalized spatial run-off trends are not shown]. The simulated run-off distribution for the southern part of Chile (35°–55°S) is in accordance with Dávila *et al.* (2002), who found the highest freshwater input through rivers to the South Eastern Pacific Ocean occurred during the period 1951–1980. In Colombia and Ecuador, river run-off is dominated by tropical climate conditions and rain (Figure 9(a)). Basins where river run-off is dominated by rain (pluvial regimes) cluster north of 40°S (Figure 9(a)). South of 40°S, including the area around the Lake District, river run-off originated from all three components (Figure 9(a)), and was highly dependent on the distribution of non-glacierized and glacierized basins combined with the presence and variability in snow and glacier coverage (Figure 9(b)), basin area and hypsometry, and climate conditions. In Chile, the relative rain contribution to river run-off is lower while snow and ice melt contributions are higher than any of the other three countries Colombia, Ecuador, and Peru (Table 2).

On an individual basin scale, in central Chile and central-western Argentina, run-off originated from snowmelt. This is in line with Masiokas *et al.* (2006) and Melo *et al.* (2010), where snowmelt is the primary source for river run-off. In the Chilean Lake District, however, the Andes Cordillera drops in elevation, and run-off originated mainly from rain [from the rainy climate conditions with Mediterranean influences (information based on, e.g. meteorological observations operated by the Dirección Meteorológica de Chile; Mernild *et al.*, 2016a)], and during the Austral winter season (June–August) (for more about the seasonal variability in run-off, see further below). Furthermore, around the Chilean Lake District

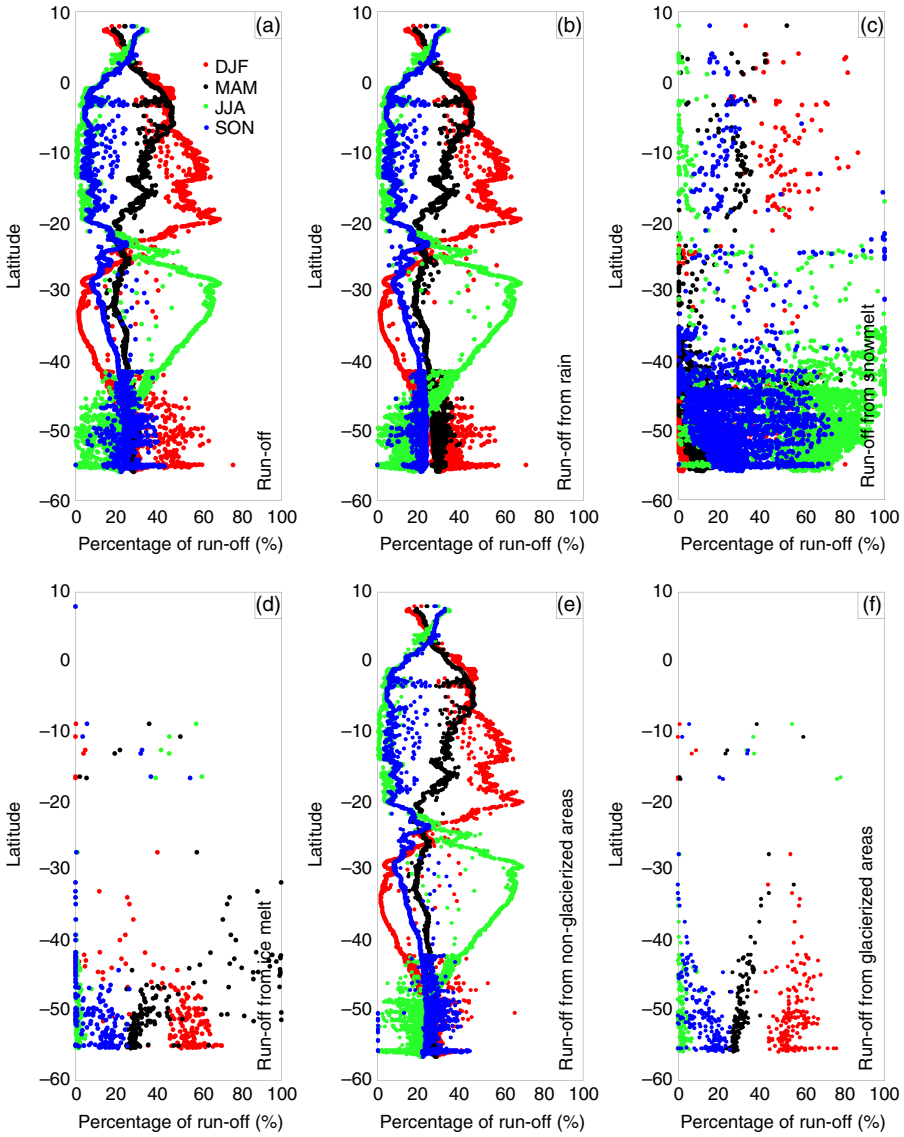

Figure 10. The percentage of seasonal basin run-off versus latitude for (a) run-off, (b) run-off from rain, (c) run-off from snowmelt, (d) run-offrun-off from ice melt, (e) run-off from non-glacierized areas, and (f) run-off from glacierized areas. The seasons are divided into three-month intervals: December, January, and February (DJF); March, April, and May (MAM); June, July, and August (JJA); and September, October, and November (SON). [Colour figure can be viewed at wileyonlinelibrary.com].

(37.5°–40°S) the simulated run-off trends (1979–2014) from each individual drainage basin outlet ($n = 75$) were, on average, slightly increasing (insignificant), where observed run-off trends (1952–2003) from selected basins ($n = 25$), on average, were decreasing (significant) (Rubio-Álvarez and McPhee, 2010); this is consistent with decreasing trends in observed precipitation. However, a direct comparison is not possible due to the differences in time periods between the simulations and streamflow records.

Regarding the lowest 35-year mean basin run-off around the arid Atacama Desert (minimum: $7.0 \pm 5.6 \times 10^4$ m^3; 22°S) no linear change in run-off trends occurred (Figures 8(a)–(f)). This is a region where the annual precipitation typically is <0.25-m w.e. (e.g. Mernild *et al.*, 2016a) and run-off from snowmelt and ice melt is negligible.

When analysing the SnowModel simulated basin-specific run-off, the 35-year mean-specific run-off and the linear trends in specific run-off both show a characteristic pattern – an hourglass shape – for the Andes Cordillera west of the continental divide (Figures 7(g) and 8(g)). Specific run-off patterns are even more pronounced towards the hourglass shape than the run-off patterns (mean and trend patterns) displayed in Figures 7(a) and 8(a). The 35-year mean simulated specific run-off shows that annual maximum specific run-off (>100 L s^{-1} km^{-2}) is present in the northern and the southern parts of the domain, and that annual minimum specific run-off (<10 L s^{-1} km^{-2}) occurs in the area around the arid Atacama Desert and south towards Santiago (Figure 7(g)). SnowModel simulations of specific run-off are in qualitative agreement with specific run-off values estimated by Cortés *et al.* (2011) obtained from several rivers on the western slopes

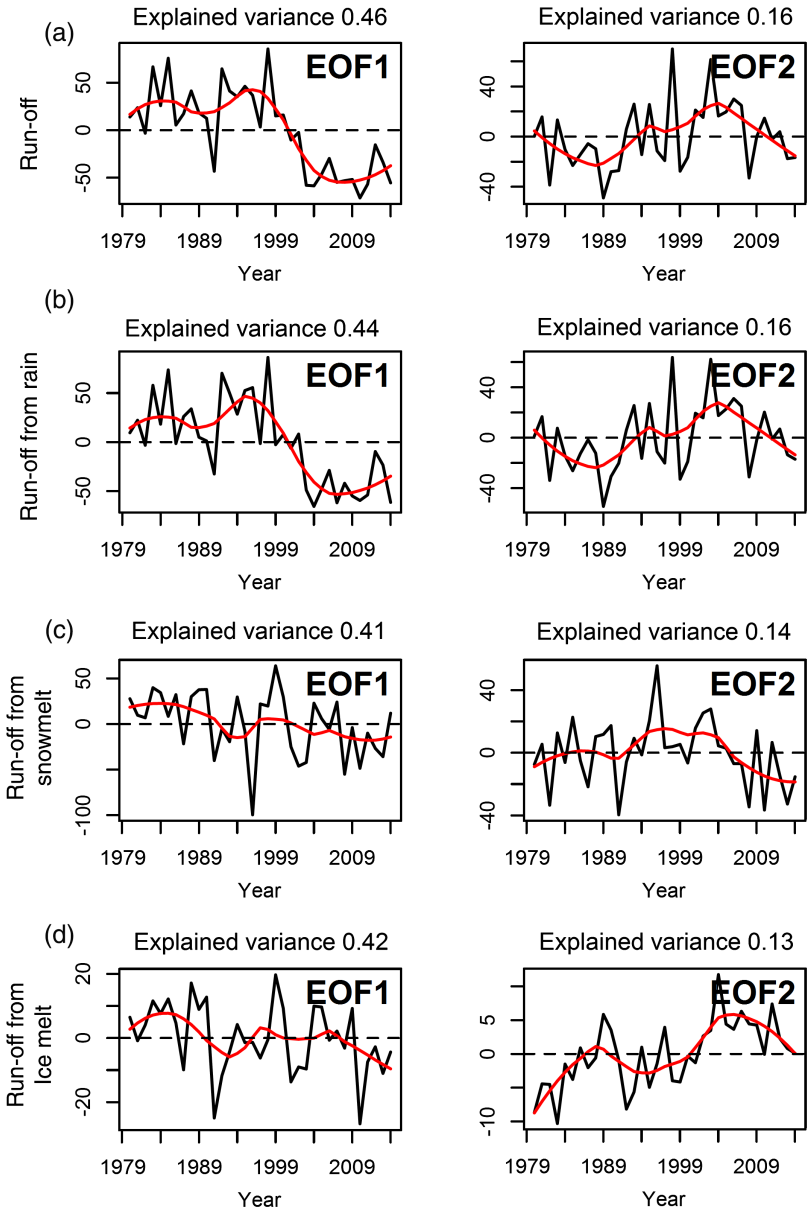

Figure 11. Simulated run-off time series (1979–2014) of the empirical orthogonal functions (black curve) and 5-year running mean smoothing line (red curve) of EOF1 and EOF2 for (a) total run-off, (b) runoff from rain, (c) run-off from snowmelt, and (d) run-off from ice melt. The explained variance is shown for each EOF. [Colour figure can be viewed at wileyonlinelibrary.com].

of the central and southern Chilean Andes Cordillera (30°–40°S; 1961–2006), spanning from ~8 L s^{-1} km^{-2} (for the Arrayan en la Montosa basin; 33.33°S) to ~65 L s^{-1} km^{-2} (for Claro en los Queñes basin; 34.98°S). A direct comparison is, however, not possible due to the differences in time periods between simulations and streamflow records. Regarding linear changes in specific run-off, the greatest changes were seen both in the north and the south of the domain (>1 L s^{-1} km^{-2} year^{-1}), and lowest changes in the centre part of the domain from the arid Atacama Desert to the area around Santiago (<0.5 L s^{-1} km^{-2} year^{-1}) (Figure 8(g)).

Figure 10(a) illustrates SnowModel-simulated run-off, rain-derived run-off, snowmelt-derived run-off, ice melt-derived run-off, run-off from non-glacierized basins, and glacierized basins along the Andes Cordillera for all seasons: winter (June–August), spring (September–November), summer (December–February), and autumn (March–May). Along the Andes Cordillera, the seasonal distribution in river run-off (here expressed in relative values) dominates in summer and autumn between 8°N and 8°S (where up to ~40% of the annual basin run-off occurs both during summer and autumn for specific basins), in summer between 8°–23°S and 45°–57°S (where up to ~60% of the annual basin run-off occurs for specific basins), and in winter between 23°S and 45°S (where up to ~60% of the annual run-off occurs for specific basins) (Figure 10(a)). This indicates a seasonal variability in run-off along the Andes Cordillera.

In addition to the seasonal variability in run-off along the Andes Cordillera, the amount of summer run-off seems to be in 'systematic' anti-phase with the amount of winter

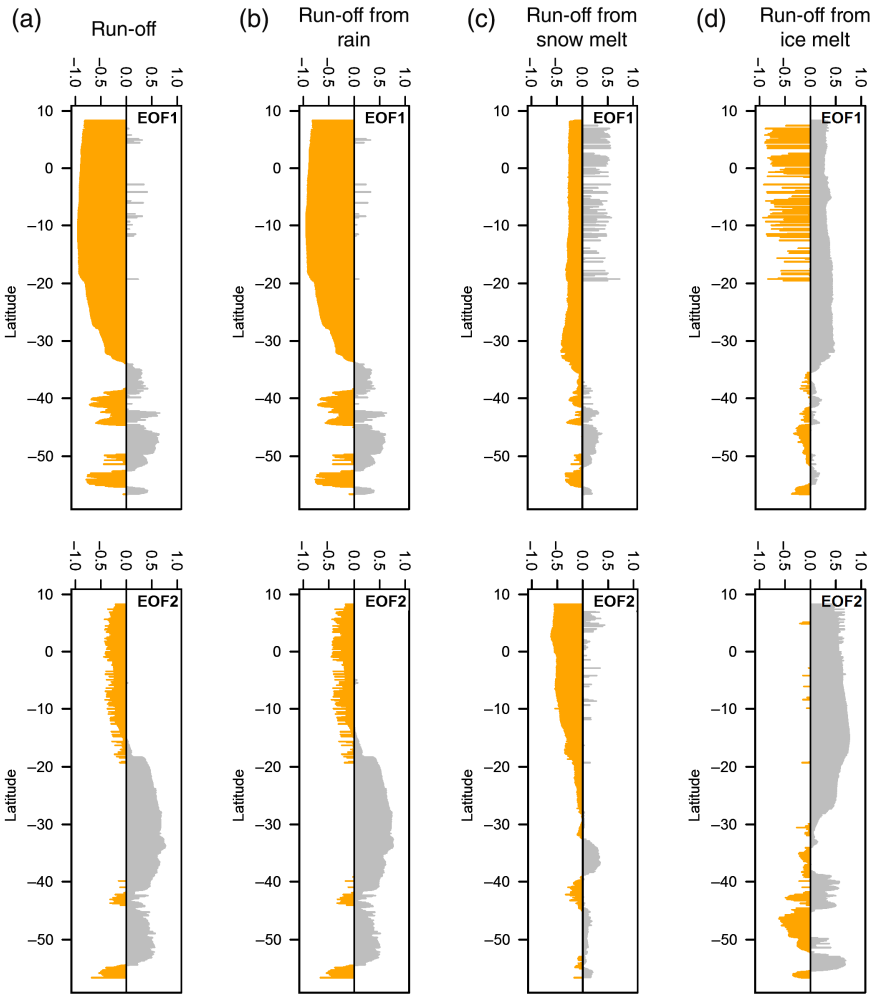

Figure 12. Eigenvector correlation values for each individual site for EOF1 and EOF2: (a) run-off, (b) run-off from rain, (c) run-off from snowmelt, and (d) run-off from ice melt. [Colour figure can be viewed at wileyonlinelibrary.com].

run-off (here expressed in relative values) (Figure 10(a)). Along the Andes Cordillera the amount of relative winter basin river run-off indicates an 'S-shaped' profile, while in contrast the amount of relative summer run-off indicates an inverse 'S-shaped' profile. During spring and autumn, the variability in run-off is less pronounced along the Andes Cordillera compared to summer and winter where seasonal variability in run-off around Atacama Desert is insignificantly different. Here, each season counts for around one quarter of the annual run-off, indicating no seasonal variability in simulated river run-off over the 35-year period (Figure 10(a)). Since rain dominates the run-off pattern for the domain, the rain-derived run-off distribution (Figure 10(b)) and the run-off non-glacierized basin distribution (Figure 10(e)) are similar to the overall seasonal run-off pattern, at least north of 40°S (Figure 10(a)). South of 40°S, run-off is dominant in winter, spring, and summer (Figures 10(c) and (d)), and originates from snow and ice melt and from glacierized basins (Figures 10(e) and (f)).

4.3. EOF river run-off variance analysis

The EOF analysis (Figures 11–13) suggests that the SnowModel simulated annual basin river run-off data set can be summarized by two major axes (modes: EOF1 and EOF2) for run-off, rain-derived run-off, snowmelt-derived run-off, and ice melt-derived run-off (Figure 11). Several assessments of significance associated with each mode (EOF; see https://github.com/marchtaylor/sinkr), implementation of North's rule and two bootstrapping methods indicate that EOF1, EOF2, and EOF3 are significant. EOF1 explains 46, 44, 41, and 42% of the explained variance in total, rain-, snow-, and ice-derived river run-off, respectively. EOF2's explained variance is lower than EOF1 for the same variables: 16, 16, 14, and 13%.

In Figure 11, we provide the temporal EOF1 and the 5-year running mean smooth total for run-off and its constituents. Smoothing lines reveal a pattern of positive values for the first ~20 years of the simulation period (1979–1999) followed by negative values (2000–2014). When EOF1 is positive, run-off is relatively low and vice versa, meaning that overall the freshwater river run-off and rain-derived run-off increase (Figure 11; Table 2). This increase in run-off was most pronounced for the last ~15 years (2000–2014) (Figure 11), and less for the first ~20 years. EOF1 thus indicates a temporal increase in both run-off parameters for the domain (Figure 11).

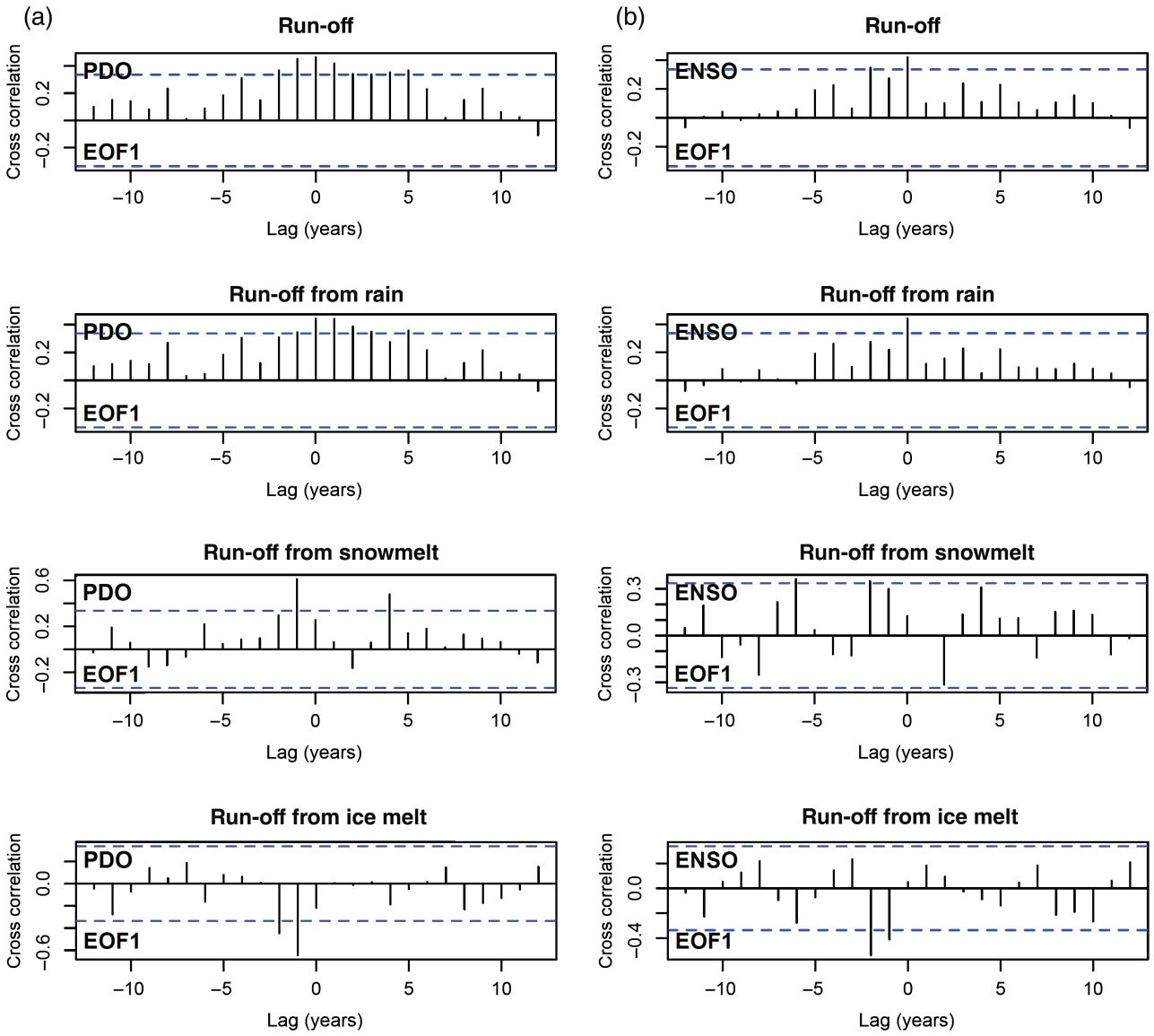

Figure 13. EOF1 cross-correlation relationships between (a) PDO and (b) ENSO for run-off, run-off from rain, run-off from snowmelt, and run-off from ice melt. The horizontal dashed lines indicate the line of significance (95% confidence). [Colour figure can be viewed at wileyonlinelibrary .com].

The temporal cycle of EOF patterns has associated spatial elements, derived from the eigenvectors (Figure 12). These eigenvectors reveal the spatial pattern in the correlation between the temporal trends captured by the EOFs and each individual basin along the Andes Cordillera (Figure 12). Overall, the temporal trend in EOF1 is shared by nearly all basins north of 30°S (as indicated by the negative correlation), and only by specific basins (or regions) south of 30°S. This indicates a geographic separation – a distinct out-of-phase variation in run-off time series in comparison to the overall domain for the last 35 years (Figures 12(a) and (b)). Snowmelt-derived run-off and ice melt-derived run-off are more diverse (Figures 12(c) and (d)) than total run-off and rain-derived run-off. We conclude that the differences in run-off patterns (including rain-derived run-off, snowmelt-derived run-off and ice melt-derived run-off) shown for the Andes Cordillera west of the continental divide are due partly to specific basin characteristics (e.g. size, aspect, elevation range, hypsometry, length of the routing network, and glacier cover), and partly due to different climate forcing functions (e.g. air temperature and precipitation) that are influenced by large-scale modes of Pacific Ocean natural variability such as ENSO and PDO (see below; Rosenblüth *et al.*, 1997; Schneider and Gies, 2004; Garreaud, 2009; Garreaud *et al.*, 2009). This is confirmed for Colombia, since the SnowModel MERRA simulations were able to reproduce the observed link between inter-annual variabilities in river run-off and ENSO (not shown) as reported by Poveda *et al.* (2001).

We also detected a pattern associated with EOF2. EOF2 has a temporal component that is roughly opposite of the temporal EOF1 pattern especially for run-off and rain-derived run-off (see Figure 11), though both patterns show approximately the same frequency. The EOF2 5-year running mean smoothing lines for run-off and rain-derived

run-off are shown to be negative for the first ∼15 years (1979–1994) and hereafter positive (Figure 11). The importance of this second pattern is in the spatial correlations of EOF2. This additional pattern is associated with a different geographic breakdown where run-off north of the Atacama Desert is negatively correlated with basin run-off located to the south; substantial basin and regional variations in annual run-off time series for South America have occurred since 1993 (Figure 12, second row). Owing to the existence of these variability patterns for EOF1 and EOF2, we suggest that variations in basin run-off along the Andes Cordillera overall can be divided into two regions (north and south of 20°–30°S), even though run-off variability for some basins within both regions will be different.

We gained further insight into the source of EOF1 and EOF 2 temporal patterns (Figure 13) via cross-correlation analysis between the EOFs and ENSO or PDO. Overall, we detected a strong immediate effect of both PDO and ENSO. In Figure 13, positive correlations between EOF1 and PDO ($r = 0.31$; significant, $p < 0.01$), and between EOF1 and ENSO ($r = 0.32$; significant, $p < 0.01$), run-off ($r = 0.31$; significant, $p < 0.01$) and rain-derived run-off ($r = 0.32$; significant, $p < 0.01$) are seen at a zero-lag. There is a real-time covariation between the pattern in EOF1 and changes in PDO and ENSO occurred. This supports the findings by Poveda *et al.* (2001), who proposed that a large-scale natural variability in ENSO is closely related to river run-off variations in Colombia.

Regarding rain-derived run-off, when both PDO and ENSO are strong, EOF1 is positive and run-off is low. Regarding snowmelt-derived run-off, it appears to be lagging behind PDO ($r = 0.60$; significant, $p < 0.01$) and ENSO ($r = 0.32$; significant, $p < 0.05$) by 1–2 years – the cause of the delay from PDO seems clear, since ENSO cycles typically remain in the same phase for 6–18 months, whereas PDO can remain in the same phase for one to two decades (Mernild *et al.*, 2015). A similar delay is observed for ice melt-derived run-off ($r = -0.61$ and $r = -0.46$; both significant and both $p < 0.01$) (Figure 13). For snowmelt-derived run-off, when both PDO and ENSO are strong and positive, EOF1 is positive, meaning a decrease in snowmelt-derived run-off. In contrast, for ice melt-derived run-off when both PDO and ENSO are strong and positive, EOF1 is negative, meaning an increase in ice melt-derived run-off. One to two years after strong PDO and ENSO years with reduced rain-derived run-off, it is likely that increasing ice melt-derived run-off and decreasing snowmelt-derived run-off will prevail. Overall, if the end-of-winter snowpack is relatively low, the start of the ablation of the underlying ice will start relative early, likely indicating a relatively low snowmelt-derived run-off and a high ice-melt-derived run-off.

4.4. Perspectives and knowledge gaps

To continue the work of understanding the links among changing climate and cryosphere and hydrosphere changes, more extensive and accurate records of the spatio-temporal river run-off for the Andes Cordillera are required to examine the links between atmosphere, terrestrial, and oceanic (hydrographic) conditions, and the potential impacts on Earth's climate system. For example, simulated run-off can be used as input in dynamic ocean models. In the Andes Cordillera and worldwide, present and projected future snow cover diminishing and glacier mass-balance loss and retreat (e.g. Liston and Hiemstra, 2011; Marzeion *et al.*, 2012; Gardner *et al.*, 2013; Mernild *et al.*, 2013, 2016a; Radić *et al.*, 2014; WGMS, 2013) raise concern about the sustainability of drinking water and irrigation supplies and hydropower production (highly relevant for glacierized basins). Future hydrological changes will likely have social health and socio-economic implications. However, in the Andes Cordillera, the majority of the river run-off regimes are pluvially controlled, emphasizing a potential effect on freshwater water resource availability due to future projected changes in climate.

This series of SnowModel papers (Parts I–IV; Mernild *et al.*, 2016a, 2016b, 2016c) has linked the conditions in the atmosphere with cryospheric and hydrological conditions in the Andes Cordillera to understand the hydrological cycle influenced by changes in precipitation, snow cover, and glacier mass balance. Even though SnowModel is a sophisticated model, more research is still needed. For instance, in the Andes Cordillera, there is still a knowledge gap regarding changes in terrestrial hydrological processes and their implications on geomorphological processes, biogeochemical weathering and nutrient fluxes, aquatic ecosystems, vegetation changes, and human interventions. By doing so, we will improve our understanding of the key socio-economic consequences of changes to the freshwater system, but we will also be able to assess the present and future potential for parts of the Andes Cordillera to become sources of freshwater for water-poor regions, such as in the Santiago de Chile and Atacama regions, where mining activities are heavily dependent on water.

5. Conclusions

A merging of SnowModel (a spatially distributed meteorological, full surface energy balance, snow and ice evolution model) and HydroFlow (a linear-reservoir run-off routing model) with NASA MERRA atmospheric forcing data was used to simulate hydrological conditions for the Andes Cordillera (west of the continental divide). The analysis included freshwater river run-off, run-off routing, and the spatio-temporal distribution of basin outlet river run-off to the surrounding fjords and seas for the 35-year period 1979 through 2014. Simulated river run-off time series were verified against DGA observed run-off time series (from the central part of Chile), showing agreement between simulations and observations.

The 35-year mean (1979–2014) gridded run-off varied considerably over distances, varying from high run-off in Colombia, Ecuador, and Patagonia to low run-off along the coastline of Peru and between the Atacama Desert and

Santiago de Chile. On average, 86% of the total run-off from the Andes Cordillera originated from rain-derived run-off, indicating, on average, a pluvial river regime. In Colombia and Chile, the proportions of rain-derived run-off were 99 and 69%, respectively. Overall, 95% of the simulated run-off originated from non-glacierized basins. Over the 35-year period, run-off changed significantly ($0.94 \times 10^{10}\,m^3\,year^{-1}$; $p < 0.01$), with the largest increases occurring in Ecuador and Colombia, whereas the increases in run-off were insignificant in Chile and Peru.

The spatial distribution of run-off from each individual drainage basin showed a 35-year mean range in basin run-off from $7.0 \pm 5.6 \times 10^{10}\,m^3$ (22°S) to $7.3 \pm 1.9 \times 10^{10}\,m^3$ (2°S), where the specific run-off pattern showed a characteristic *hourglass shape* for the Andes Cordillera with specific run-off values $>100\,L\,s^{-1}\,km^{-2}$ for the northern and southern parts of the Andes Cordillera, and $<10\,L\,s^{-1}\,km^{-2}$ around the arid Atacama Desert. Furthermore, a distribution of basin run-off into rain-derived run-off, snowmelt-derived run-off, and ice melt-derived run-off emphasized that basins dominated by rain-derived run-off were primarily located north of 40°S, and that south of 40°S basin river run-off originated from all three components.

Mapping and understanding the spatio-temporal river run-off conditions for the Andes Cordillera (west of the continental divide) are of interest for our understanding of a changing climate and changes in the cryosphere and hydrosphere (as described in these SnowModel Parts I–IV papers; Mernild *et al.*, 2016a, 2016b, 2016c). Models of hydrological conditions and variability are important for understanding key socio-economic consequences of changes to the freshwater system and freshwater conditions as a source for water-poor regions.

Acknowledgements

We thank the anonymous reviewers for their valuable reviews and their insightful critique of this article. This work was supported by the National Science Foundation of Chile *Fondecyt* under Grant Agreement #1140172. All model data requests should be addressed to the first author. We thank Direction General de Aguas for providing observed river run-off time series from Chile. The authors have no conflict of interest.

References

AMAP. 2011. Chapter 7: mountain glaciers and ice caps. In *Snow, Water, Ice and Permafrost in the Arctic (SWIPA): Climate Change and the Cryosphere*. Arctic Monitoring and Assessment Program (AMAP): Oslo, 61 pp., xii + 538 pp.

Ayala A, McPhee J, Vargas X. 2014. Altitudinal gradients, midwinter melt, and wind effects on snow accumulation in semiarid mid-latitude Andes under La Niña conditions. *Water Resour. Res.* **50**: 3589–3594, doi: 10.1002/2013WR01496.

Baraer M, Mark B, McKenzie J, Condom T, Bury J, Huh K-I, Portocarrero C, Gomez J, Rathay S. 2012. Glacier recession and water resources in Peru's Cordillera Blanca. *J. Glaciol.* **58**(207): 134–150, doi: 10.3189/2012JoG11J186.

Beamer JP, Hill DF, Arendt A, Liston GE. 2016. High-resolution modeling of coastal freshwater discharge and glacier mass balance in the Gulf of Alaska watershed. *Water Resour. Res.* **52**: 3888–3909, doi: 10.1002/2015WR018457.

Bliss A, Hock R, Radić V. 2014. Global response of glacier runoff to twenty-first century climate change. *J. Geophys. Res. Earth Surf.* **119**: 717–730, doi: 10.1002/2013JF002931.

Bosilovich MG. 2008. NASA's modern era retrospective analysis for research and applications: integrating earth observations. *Earthzine*. http://www.earthzine.org/2008/09/26/nasas-modern-era-retrospective-analysis/ (accessed 12 October 2016).

Bosilovich MG, Chen J, Robertson FR, Adler RF. 2008. Evaluation of global precipitation re-analyses. *J. Appl. Meteorol. Climatol.* **47**: 2279–2299, doi: 10.1175/2008JAMC1921.1.

Bosilovich MG, Franklin RR, Chen J. 2011. Global energy and water budgets in MERRA. *J. Clim.* **24**: 5721–5739, doi: 10.1175/2011JCLI4175.1.

Carrasco JF, Casassa G, Quintana J. 2005. Changes of the 0 °C isotherm and the equilibrium line altitude in the central Chile during the last quarter of the 20th century. *Hydrol. Sci. J.* **50**(6): 933–948, doi: 10.1623/hysj.2005.50.6.933.

Cornwell E, Molotch NP, McPhee J. 2016. Spatio-temporal variability of snow water equivalent in the extra-tropical Andes Cordillera from distributed energy balance modeling and remotely sensed snow cover. *Hydrol. Earth Syst. Sci.* **20**: 411–430, doi: 10.5194/hess-20-411-2016.

Cortés G, Vargas X, McPhee J. 2011. Climatic sensitivity of streamflow timing in the extratropical western Andes Cordillera. *J. Hydrol.* **405**(1): 93–109.

Crespo P, Feyen J, Buytaert W, Bücker A, Breuer L, Frede HG, Ramírez M. 2011. Identifying controls of the rainfall–runoff response of small catchments in the tropical Andes (Ecuador). *J. Hydrol.* **407**(1–4): 164–174, doi: 10.1016/j.jhydrol.2011.07.021.

Cullather RI, Bosilovich MG. 2011. The moisture budget of the polar atmosphere in MERRA. *J. Clim.* **24**: 2861–2879, doi: 10.1175/2010JCLI4090.1.

Danielson, JJ, Gesch, DB. 2011. Global multi-resolution terrain elevation data 2010 (GMTED2010). U.S. Geological Survey Open-File Report 2011–1073, 26 pp.

Dávila PM, Figueroa D, Uller EM. 2002. Freshwater input into the coastal ocean and its relation with the salinity distribution offaustral Chile (35–55°S). *Cont. Shelf Res.* **22**(3): 521–534.

Escobar F, Casassa G, Pozo V. 1995. Variaciones de un glaciar deMontaña en los Andes de Chile Central en las últimas dos décadas. *Bull. Inst. Fr. Etudes Andines* **24**(3): 683–695.

Favier V, Falvey M, Rabatel A, Praderio E, López D. 2009. Interpreting discrepancies between discharge and precipitation in high-altitude area of Chile's Norte Chico region (26–32°S). *Water Resour. Res.* **45**(2): 1–20, doi: 10.1029/2008WR006802.

Fleischbein K, Wilcke W, Valarezo C, Zech W, Knoblich K. 2006. Water budgets of three small catchments under montane forest in Ecuador: experimental and modelling approach. *Hydrol. Process.* **20**(12): 2491–2507.

Gardner AS, Moholdt G, Cogley JG, Wouters B, Arendt AA, Wahr J, Berthier E, Hock R, Pfeffer WT, Kaser G, Ligtenberg SRM, Bolch T, Sharp MJ, Hagen JO, van den Broeke M, Paul F. 2013. A reconciled estimate of glacier contribution to sea level rise: 2003 to 2009. *Science* **340**: 852–857.

Garreaud RD. 2009. The Andes climate and weather. *Adv. Geosci.* **7**: 1–9.

Garreaud RD, Vuille M, Compagnucci R, Marengo J. 2009. Present-day South American climate. *Palaeogeogr. Palaeoclimatol. Palaeoecol.* **281**(3–4): 180–195.

Gascoin S, Kinnard C, Ponce R, Macdonell S, Lhermitte S, Rabatel A. 2011. Glacier contribution to streamflow in two headwaters of the Huasco River, Dry Andes of Chile. *Cryosphere* **5**: 1099–1113.

Gordon RP, Lautz LK, McKenzie JM, Mark BG, Chavez D, Baraer M. 2015. Sources and pathways of stream generation in tropical proglacial valleys of the Cordillera Blanca, Peru. *J. Hydrol.* **522**: 628–644, doi: 10.1016/j.jhydrol.2015.01.013.

Hall DK, Riggs GA. 2007. Accuracy assessment of the MODIS snow products. *Hydrol. Process.* **21**: 1534–1547, doi: 10.1002/hyp.6715.

Hall DK, Riggs GA, Salomonson VV. 1995. Development of methods for mapping global snow cover using Moderate Resolution Imaging Spectroradiometer (MODIS) data. *Remote Sens. Environ.* **54**: 127–140.

Hall DK, Salomonson VV, Riggs GA. 2006. *MODIS/Terra Snow Cover Daily L3 Global 500 m Grid. Version 5. Fractal Snow Cover*. NASA National Snow and Ice Data Center Distributed Active Archive Center: Boulder, CO.

Hock R, Jansson P, Braun L. 2005. Modelling the response of mountain glacier discharge to climate warming. In *Global Change and Mountain Regions – A State of Knowledge Overview*, Huber UM, Reasoner MA, Bugmann H (eds). Springer: Dordrecht, The Netherlands, 243–252.

Jansson P, Hock R, Schneider T. 2003. The concept of glacier water storage – a review. *J. Hydrol.* **282**(1–4): 116–129, doi: 10.1016/S0022-1694(03)00258-0.

Kapnick and Hall , 2012.

Le Quesne C, Acuna C, Boninsegna JA, Rivera A, Barichivich J. 2009. Long-term glacier variations in the Central Andes of Argentina and Chile, inferred from historical records and tree-ring reconstructed precipitation. *Palaeogeogr. Palaeoclimatol. Palaeoecol.* **281**(3–4): 334–344.

Liston GE. 1995. Local advection of momentum, heat, and moisture during the melt of patchy snow covers. *J. Appl. Meteorol.* **34**: 1705–1715, doi: 10.1175/1520-0450-34.7.1705.

Liston GE, Elder K. 2006a. A meteorological distribution system for high-resolution terrestrial modeling (MicroMet). *J. Hydrometeorol.* **7**: 217–234, doi: 10.1175/JHM486.1.

Liston GE, Elder K. 2006b. A distributed snow-evolution modeling system (SnowModel). *J. Hydrometeorol.* **7**: 1259–1276, doi: 10.1175/JHM548.1.

Liston GE, Hiemstra CA. 2011. The changing cryosphere: pan-Arctic snow trends (1979–2009). *J. Clim.* **24**: 5691–5712.

Liston GE, Mernild SH. 2012. Greenland freshwater runoff. Part I: a runoff routing model for glaciated and non-glaciated landscapes (HydroFlow). *J. Clim.* **25**(17): 5997–6014.

Liston GE, Sturm M. 1998. A snow-transport model for complex terrain. *J. Glaciol.* **44**: 498–516.

Liston GE, Sturm M. 2002. Winter precipitation patterns in Arctic Alaska determined from a blowing-snow model and snow depth observations. *J. Hydrometeorol.* **3**: 646–659.

Liston GE, Winther J-G, Bruland O, Elvehøy H, Sand K. 1999. Below surface ice melt on the coastal Antarctic ice sheet. *J. Glaciol.* **45**: 273–285, doi: 10.3189/002214399793377130.

Liston GE, Haehnel RB, Sturm M, Hiemstra CA, Berezovskaya S, Tabler RD. 2007. Simulating complex snow distributions in windy environments using SnowTran-3D. *J. Glaciol.* **53**: 241–256.

López-Moreno JI, Fontaneda S, Bazo J, Revuelto J, Azorin-Molina C, Valero-Garcés B, Morán-Tejeda E, Vicente-Serrano SM, Zubieta R, Alejo-Cochachín J. 2014. Recent glacier retreat and climate trends in Cordillera Huaytapallana, Peru. *Glob. Planet. Change* **112**: 1–11.

Malmros JK, Mernild SH, Wilson R, Fensholt R, Yde JC. 2016. Glacier changes in the Rio Olivares catchment, central Chilean Andes, 1955–2013. *J. Glaciol.* **62**(232): 391–401, doi: 10.1017/jog.2016.43.

Marzeion B, Jarosch AH, Hofer M. 2012. Past and future sea-level change from the surface mass balance of glaciers. *Cryosphere* **6**: 1295–1322, doi: 10.5194/tc-6-1295-2012.

Masiokas MH, Villalba R, Luckman BH, Le Quesne C, Aravena JC. 2006. Snowpack variations in the central Andes of Argentina and Chile, 1951–2005: large-scale atmospheric influences and implications for water resources in the region. *J. Clim.* **19**(24): 6334–6352.

McClung DM. 2013. The effects of El Niño and La Niña on snow and avalanche patterns in British Columbia, Canada, and central Chile. *J. Glaciol.* **59**(216): 783–792.

Melo O, Vargas X, Vicuna S, Meza F, McPhee J. 2010. Climate change economic impacts on supply of water for the M & I sector in the Metropolitan Region of Chile. *Watershed Manag.* 159–170, doi: 10.1061/41143(394)15.

Mernild SH. 2006. The internal drainage system of the lower Mittivakkat Glacier, Ammassalik Island, SE Greenland. *Dan. J. Geogr.* **106**: 13–24.

Mernild SH, Liston GE. 2012. Greenland freshwater runoff. Part II: distribution and trends, 1960–2010. *J. Clim.* **25**(17): 6015–6035.

Mernild SH, Hasholt B, Liston GE. 2006. Water flow through Mittivakkat Glacier, Ammassalik Island, SE Greenland. *Dan. J. Geogr.* **106**: 25–43.

Mernild SH, Lipscomb WH, Bahr DB, Radić V, Zemp M. 2013. Global glacier retreat: A revised assessment of committed mass losses and sampling uncertainties. *The Cryosphere* **7**: 1565–1577, doi: 10.5194/tc-7-1565-2013.

Mernild SH, Liston GE, Hiemstra CA. 2014. Northern hemisphere glaciers and ice caps surface mass balance and contribution to sea-level rise. *J. Clim.* **27**(15): 6051–6073, doi: 10.1175/JCLI-D-13-00669.1.

Mernild SH, Beckerman AP, Yde JC, Hanna E, Malmros JK, Wilson R, Zemp M. 2015. Mass loss and imbalance of glaciers along the Andes to the sub-Antarctic islands. *Glob. Planet. Change* **133**: 109–119, doi: 10.1016/j.gloplacha.2015.08.009.

Mernild SH, Liston GE, Hiemstra CA, Malmros JK, McPhee J. 2016a. The Andes Cordillera. Part I: snow distribution, properties, and trends (1979–2014). *Int. J. Climatol.*, doi: 10.1002/joc.4804.

Mernild SH, Liston GE, Hiemstra CA, Yde JC, McPhee J, Malmros JK. 2016b. The Andes Cordillera. Part II: Rio Olivares Basin snow conditions (1979–2014), central Chile. *Int. J. Climatol.*, doi: 10.1002/joc.4828.

Mernild SH, Liston GE, Hiemstra CA, Wilson R. 2016c. The Andes Cordillera. Part III: glacier surface mass balance and contribution to sea level rise (1979–2014). In review. *Int. J. Climatol.* 1–21, doi: 10.1002/joc.4907.

Montecinos A, Aceituno P. 2002. Seasonality of the ENSO-related rainfall variability in central Chile and associated circulation anomalies. *J. Clim.* **16**: 281–296.

Nash JE, Sutcliffe JV. 1970. River flow forecasting through conceptual models, part I – a discussion of principles. *J. Hydrol.* **10**: 282–290.

Paruelo JM, Beltran A, Jobbagy E, Sala OE, Golluscio RA. 1998. The climate of Patagonia: general patterns and controls on biotic processes. *Ecol. Aust.* **8**: 85–101.

Pfeffer WT, Arendt AA, Bliss A, Bolch T, Cogley JG, Gardner AS, Hagen J-O, Hock R, Kaser G, Kienholz C, Miles ES, Moholdt G, Molg N, Paul F, Radić V, Rastner P, Raup BH, Rich J, Sharp MJ, The Randolph Consortium. 2014. The Randolph Glacier Inventory: a globally complete inventory of glaciers. *J. Glaciol.* **60**(221): 537–552.

Poveda G, Jaramillo A, Gil MM, Quiceno N, Mantilla RI. 2001. Seasonally in ENSO-related precipitation, river discharges, soil moisture, and vegetation index in Colombia. *Water Resour. Res.* **37**(8): 2169–2178.

Preisendorfer RW. 1998. In *Principal Component Analysis in Meteorology and Oceanography*, Mobley CD (ed). Elsevier: Amsterdam, 452.

Radić V, Bliss A, Beedlow RA, Hock R, Miles E, Cogley JG. 2014. Regional and global projection of twenty-first century glacier mass changes in response to climate scenarios from global climate models. *Clim. Dyn.* **42**: 37–58, doi: 10.1007/s00382-013-1719-7.

Rienecker MM, Suarez MJ, Gelaro R, Todling R, Bacmeister J, Liu E, Bosilovich MG, Schubert SG, Takacs L, Kim G-K, Bloom S, Chen J, Collins D, Conaty A, Silva Ad, Gu W, Joiner J, Koster RD, Lucchesi R, Molod A, Owens T, Pawson S, Pegion P, Redder CR, Reichle R, Robertson FR, Ruddick AG, Sienkiewicz M, Woollen J. 2011. MERRA: NASA's modern-era retrospective analysis for research and applications. *J. Clim.* **24**: 3624–3648, doi: 10.1175/JCLI-D-11-00015.1.

Robertson FR, Bosilovich MG, Chen J, Miller TL. 2011. The effect of satellite observing system changes on MERRA water and energy fluxes. *J. Clim.* **24**: 5197–5217, doi: 10.1175/2011JCLI4227.1.

Romero, H. 1985. *Geografıa de los Climas*, Tomo XI. Instituto Geografico Militar: Geografıa de Chile, 243 pp.

Rosenblüth B, Fuenzalida HA, Aceituno P. 1997. Recent temperature variations in Southern South America. *Int. J. Climatol.* **17**: 67–85.

Rubio-Álvarez E, McPhee J. 2010. Patterns of spatial and temporal variability in streamflow records in south central Chile in the period 1952–2003. *Water Resour. Res.* **46**(5): 1–16, doi: 10.1029/2009WR007982.

Rutllant J, Fuenzalida H. 1991. Synoptic aspects of the central Chile rainfall variability associated with the southern oscillation. *Int. J. Climatol.* **11**(1): 63–76.

Sagredo EA, Lowell TV. 2012. Climatology of Andean glaciers: a framework to understand glacier response to climate change. *Glob. Planet. Change* **86–87**: 101–109.

Saltzmann N, Huggel C, Rohrer M, Silverio W, Mark BG, Burns P, Portocarrero C. 2013. Glacier changes and climate trends derived from multiple sources in the data scarce Cordillera Vilcanota region, Southern Peruvian Andes. *Cryosphere* **7**: 103–118, doi: 10.5194/tc-7-103-2013.

Schneider C, Gies D. 2004. Effects of El Niño-Southern Oscillation on southernmost South America precipitation at 53°S revealed from NCEP–NCAR reanalysis and weather station data. *Int. J. Climatol.* **24**: 1057–1076.

Sparnocchia S, Pinardi N, Demirov E. 2003. Multivariate empirical orthogonal function analysis of the upper thermocline structure of the Mediterranean Sea from observations and model simulations. *Ann. Geophys.* **21**: 167–187.

Vaughan DG, Comiso JC, Allison I, Carrasco J, Kaser G, Kwok R, Mote P, Murray T, Paul F, Ren J, Rignot E, Solomina O, Steffen K, Zhang T. 2013. Observations: cryosphere. In *Climate Change 2103: The Physical Science Basis. Contribution of Working Group I to the*

Fifth Assessment Report of the Intergovernmental Panel on Climate Change, Stocker TF, Qin D, Plattner G-K, Tignor M, Allen SK, Boschung J, Nauels A, Xia Y, Bex V, Midgley PM. (eds). Cambridge University Press: Cambridge, UK and New York, NY, 317–382.

Veettil BK, Maier ELB, Bremer UF, de Souza SF. 2014. Combined influence of PDO and ENDO on Northern Andean glaciers: a case study on the Cotopaxi ice-covered volcano, Ecuador. *Clim. Dyn.* **43**(12): 3439–3448, doi: 10.1007/s00382-014-2114-8.

Wolter K, Timlin MS. 2011. El Niño/Southern Oscillation behaviour since 1871 as diagnosed in an extended multivariate ENSO index (MEI.ext). *Int. J. Climatol.* **31**(7): 1074–1087.

World Glacier Monitoring Service (WGMS). 2013. *Glacier Mass Balance Bulletin 2010–2011*, Vol. 12, Zemp M, Nussbaumer SU, Naegeli K, Gärtner-Roer I, Paul F, Hoelzle M, Haeberli W (eds). ICSU (WDS)/IUGG (IACS)/UNEP/UNESCO/WMO, World Glacier Monitoring Service: Zurich, Switzerland, 106 pp., publication based on database version. doi: 10.5904/wgms-fog-2013-11.

Yuan XJ, Martinson DG. 2000. Antarctic sea ice extent variability and its global connectivity. *J. Clim.* **13**(10): 1697–1717.

Yuan XJ, Martinson DG. 2001. The Antarctic dipole and its predictability. *Geophys. Res. Lett.* **28**(18): 3609–3612.

Zhang Y, Wallace JM, Battisti DS. 1997. ENSO-like inter-decadal variability: 1900–93. *J. Clim.* **10**: 1004–1020, doi: 10.1175/1520-0442(1997).

